From single to multi-stage forming process of copper thin sheet

Amine Lagroum, Pierre-Yves Manach, Sandrine Thuillier

Mechanics & Industry **26**, 4 (2025)

https://doi.org/10.1051/meca/2024039

Mechanics & Industry

Available online at:
www.mechanics-industry.org

ORIGINAL ARTICLE

OPEN ACCESS

From single to multi-stage forming process of copper thin sheet

Amine Lagroum*, Pierre-Yves Manach, and Sandrine Thuillier

Univ. Bretagne Sud, UMR CNRS 6027, IRDL, 56100 Lorient, France

Received: 1 October 2024 / Accepted: 21 December 2024

Abstract. In the electronics industry sector, different types of parts made out of copper alloys are used, such as metal supports (lead frames), on which the chips are assembled. These parts are produced using progressive dies, with several blanking and bending stages. There is a huge interest to numerically predict these multi-stage forming processes, to decrease design time and to anticipate production problems such as non-compliance with dimensional tolerances depending on the material used. This paper deals with the progressive forming of copper parts with single and multi-stage process coupled with experimental and numerical approaches for bending operations. The main contribution of this study is the design of a single stage bending tool for rectangular samples representative of multi-stage industrial processes, providing a relevant experimental database for numerical model validation. This device is based on the technology of progressive dies, though it allows the production of one part at a time. Instrumentation provides local load and displacement and an experimental database is built for Cu-ETP R290 copper strip. A multi-stage bending industrial process dedicated to the manufacturing of electrical contacts is also considered in this study. Numerical models of both single and multi-stage processes are developed, with a focus on the technological importance of a cam slider for the industrial process. The results show that the bending force is mainly influenced by the sample width. In addition, numerical models for the rectangular geometries capture some of the trends from the experiment such as the proportionality of the maximum force with the bent width. Overall, the models are able to predict springback within the process tolerance. Finally, comparison of one stage of the bending sequence with the single stage bending model showed that the single model approach gives similar results in terms of load and plastic deformation.

Keywords: Copper sheet / bending / progressive dies / experiment / finite element.

1 Introduction

The progressive forming of copper alloy sheets, with thickness ranging from a few tenths to one millimeter, is a widespread process in the electronic industry. The manufacturing of these parts is based on the use of progressive tools (also called progressive dies) for blanking operations generally followed by forming, essentially bending operations [1]. The progressive tool is divided into several stations, each station corresponding to one or more operations. The particularity of this type of process is that the part remains attached to the metal strip, which carries the part and controls the alignment, from one operation to the following one; the part is cut out of the strip at the last operation. The specifications impose high production rates and increasingly strict dimensional tolerances on the parts produced, which requires a fine control of the progressive forming process. However, the design of progressive tools is essentially based on empirical rules and the know-how of operators.

A first level approach to reduce the design time [2] and to improve the part quality is the development of computer-aided design (CAD) and manufacturing (CAM) systems for progressive tools. These systems lead to an automation of the design of progressive tools for sheet metal products with complex shape obtained by blanking, bending [3] and deep drawing operations [4]. They use knowledge-based rules, Artificial Intelligence approach [5] and scrap reduction [6]. Progressive tools design with mainly bending operations was particularly addressed [7], e.g., to minimize the number of stations of the tool [8] and the torque difference between the two sides of the die, as it can extend tool life [9]. Numerical simulation of progressive processes taking into account plastic deformation is time consuming and is therefore rarely used during design phases of progressive tools. One of the first study to use numerical simulation was related to the prediction of defects as cracks during die design for strip layout design and tool design, by coupling CAD and the finite element

* e-mail: amine.lagroum@gmail.com

software DEFORM[1] [10]. More recently, some studies have been dedicated to industrial process improvement, as a tool failure prevention approach for progressive die stamping based on the continuous monitoring of the local loads with sensors [11] and the reduction of strip vibration during progressive die stamping, as it can have an influence on the part quality [12]. Integration of numerical simulation into tool design is still recent, with the objective to improve the material flow [13], to anticipate production problems such as fracture or non-compliance with dimensional tolerances depending on the material used [14] and to decrease scrap production, which is essential for a sustainable use of copper and its alloys [15].

For electronic components, bending is an essential step and dimensional accuracy is of utmost importance for the following assembly steps. This study focuses on the accurate prediction of the bending of copper parts using progressive tools for applications related to the electronic industry. In this context, electrical contacts are essentially bent at 90° along a straight edge.

During the bending process, also called L-bending, wipe-bending or flanging, one end of the sheet is held between a die and a blank holder and the other free end is pushed by the action of a punch towards the die radius to form the bent area of the part [16], cf. Figure 1a. The bending operation is characterized by several geometric parameters, such as the die and punch radii and the punch/die clearance. The bent height and the bending angle measured after the tools removal are the output data, cf. Figure 1b.

The characteristic force evolution during bending, cf. Figure 1a, is divided into several phases [17]: firstly, bending of the sheet around the die radius to which frictional forces will be added. Then, the force drops significantly as the bending radius is practically formed and the bent edge moves closer to the die. Finally, a constant force is recorded, which is related to the friction between the sheet and the punch [18]. In the case of straight edge bending, experiments carried out with steel sheets showed that a decrease in the punch radius R_p results in an increase of the bending force [19]; and the bending radius is formed in a quicker way. A decrease of the force with an increasing punch/die clearance has also been observed.

Springback affects the final shape of the part when the punch is removed, cf. Figure 1b. This phenomenon is influenced by punch and die radii, punch/die clearance, blank holder force as well as by the material (mechanical properties and thickness). An increase in tool radii or clearance will result in an increase in springback [20]. Moreover, a comparison of copper in a semi-hard metallurgical state with a hard metallurgical state shows that springback increases as the hardness of the material increases. There is also an influence of the bending direction on the springback magnitude, as it is higher when bending is performed along the direction (rolling or transverse one) in which the mechanical properties are higher [21]. Control of the bent angle is of utmost importance and compensation strategies have been tested, like overbending with a cam slider

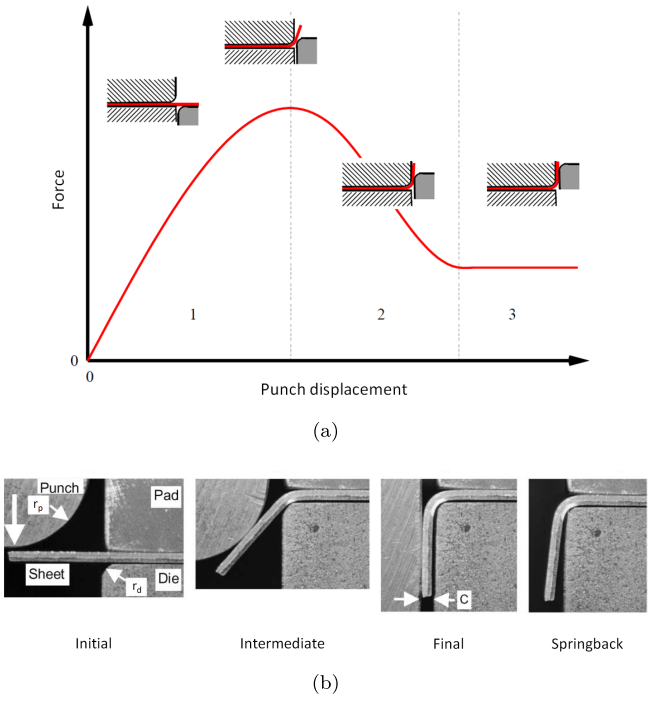

Fig. 1. (a) Characteristic force-displacement curve for bending (flanging) (adapted from [17]); (b) Springback after bending (adapted from [19]).

to adjust the punch movement or transversal compression drawing using sliders [22].

The numerical modeling of wipe-bending in general is scarcely discussed in literature, except for flanging, which is the first step prior to the hemming process. Previous studies mainly dealt with steels (0.67–1.18 mm) [23] or aluminum alloys (1–1.2 mm) [17]. However, the flanging operation is usually not very detailed and case studies dealing with copper alloys were not addressed. Numerical models of the bending operation are developed in 2D plane strain [24], e.g., with DEFORM2D within an implicit scheme (steel 0.838 mm) [25] or in 3D [26], in case of the bending of a holed sample (steel 4 mm) [27] or with Abaqus/Standard [28], to optimize the parameters of the bending process to minimize damage in the bent parts.

Material models, within a phenomenological approach, range from simple isotropic hardening coupled with von Mises yield criterion [29] to an advanced mixed hardening model coupled with an anisotropic yield criterion [30]. This last one was used for the 3D modeling of a bending stage of a progressive micro-forming process making use of a copper alloy (CuBe2 1/4H 0.1 mm).

The predicted force-displacement curve and springback magnitude depend strongly on the mesh size and a compromise between accuracy and computation time must be reached [31]. The number of layers of elements in the thickness of the sheet is variable, ranging from 4 to 16 layers of elements in the thickness [18]. The ratio $r/3.8$ [27], respectively $r/6.4$ [32], is used to define the size and the number of elements to describe the radii r of the tools.

Concerning friction, Coulomb's law is most often used to model the mechanical behavior of the interfaces

[1] https://www.deform.com/

between the deformable sheet and the rigid tools for bending. Most often, the friction coefficients are chosen to be as close as possible to the experimental conditions (with or without lubrication) based on the literature findings [33]. Tribological tests representative of the bending tests were also performed [18]. Moreover, during force instrumented hemming tests, friction coefficients were calculated from the measurement of vertical and horizontal force during the hemming operation [23]. As an alternative, the final plateau on the load-displacement curve is related to the friction between the sheet and the punch and can be used to fix the friction coefficient [17].

The clearance between the punch and the die is an important parameter. The gap value may not be constant during the whole process, due to tool deformation, and a rigid tool may lead to an overestimation of the load [19]. The authors propose an adjustment of the clearance to be applied to the numerical model. An alternative is to use deformable tools [34]. It comes that, though the process itself is rather simple to model, input data, that are not accurately controlled during the experiments, like the punch/die clearance, have a significant influence.

As a conclusion, most studies on progressive processes have focused on improving CAD/CAM systems to save design time. However, numerical simulation of multi-stage processes is practically absent from design phases. And bending is most often associated with flanging of steel and aluminum alloys sheets for the automotive industry while bending of copper sheets for electrical applications is scarcely addressed. Different geometrical or technological parameters can influence the load evolution and the springback magnitude but numerical prediction of bending, especially springback, is not often presented. Hence, this paper deals with the progressive forming of copper parts with single and complex process coupled with experimental and numerical approaches for bending operations.

The main contribution of this study is the design of a single stage bending tool for rectangular samples representative of several bending operations of multi-stage industrial processes in the electronic industry, providing a relevant experimental database for numerical model validation. An original instrumented bending tool was specifically designed to be representative of a single stage tool in industrial environment. This device is based on the technology of progressive tools, though it allows the production of one part at a time. Instrumentation provides local load and displacement and an experimental database is built for Cu-ETP R290 copper strip with a nominal thickness of 0.8 mm. A multi-stage bending process from an industrial tool, dedicated to the manufacturing of electrical contacts, is also considered in this study. Numerical models of both single and multi-stage processes are developed, with a focus on the technological importance of a cam slider for the industrial process.

This paper is organized as follows: Section 2 deals with the material, the experimental procedure and the numerical models of the bending processes. Then, Section 3 details the results obtained, focused on a comparison between experiments and numerical predictions for the load and springback magnitude. Moreover, the influence of the cam slider on the springback magnitude is analysed, and a comparison between the single stage bending process and the industrial one is presented. Finally, the main conclusions are summarized in Section 4.

2 Experimental and numerical methods

This section first introduces the material of the study. Next, the single stage bending tool is presented, as well as the methods used to characterize bending in terms of force, springback and strain field, as well as the multi-stage process. Finally, the numerical models are detailed, with a focus on the calibration of input parameters such as the friction coefficient and the punch/sheet clearance, based on the load evolution and level, for the single stage process.

2.1 Material

The material used in this study is a commercially pure copper (99.9%) Cu-ETP (Electrolytic Tough Pitch), provided in coils cut into strips with a nominal thickness t_0 of 0.8 mm and a nominal width of 85.5 mm. The material is received in a metallurgical state R290, corresponding to the following specifications: $R_{p0.2\%} \geq 250$ MPa, R_m in the range 290-360 MPa. The tests for the single and multi-stage processes are both made with the same material but from 2 different coils. Tensile tests, with a standard geometry of ASTM-E8/E8M, were performed in the rolling direction under quasi-static conditions, using digital image correlation to measure the local strain tensor. The hardening curve shown in Figure 2 was obtained by using an interpolation of a local strain measure within the necking area up to an equivalent plastic strain of 0.5, for equivalent plastic strains in-between 0 and 0.5, the stress level evolves from 300 MPa up to 420 MPa. Young's modulus and Poisson's ratio are respectively 105.1 GPa and 0.28.

The copper behavior is modeled using isotropic hardening coupled with von Mises yield criterion. Although the normal anisotropy coefficient is 0.61, anisotropy is not taken into account in a first stage. It was shown that the stress levels at 0°, 45° and 90° are rather similar [35] and this assumption is expected to influence mainly the thickness distribution at the end of the forming stage. Maximum strain rates in bending can reach 13 s^{-1} and 30 s^{-1} for the single stage and multi-stage processes respectively. However, copper has a moderate strain rate sensitivity between 0.001 s^{-1} and 10 s^{-1}, as evidenced by several authors [36], with a stress increase around 30 MPa over 4 decades of strain rates. Therefore, the strain hardening curve obtained at a strain rate of 0.001 s^{-1} is taken as a good representation of the mechanical behavior of the material during the forming process. The maximum equivalent plastic strain reached during the bending process is around 0.4 and rupture never occurred during the experiments. Therefore, nor damage nor an uncoupled rupture criterion were considered in this study.

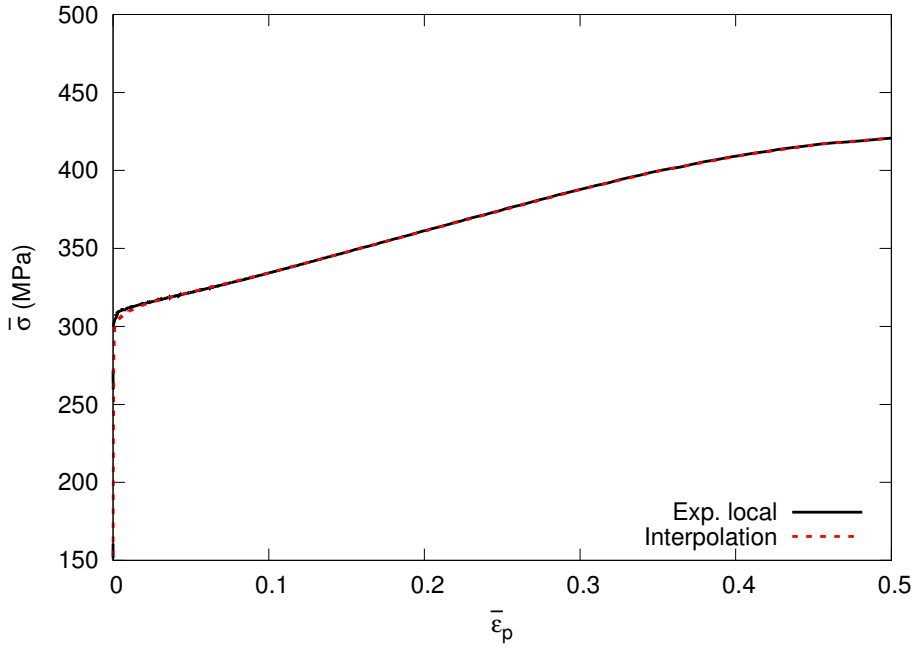

Fig. 2. Strain hardening law of Cu-ETP R290 copper from a tensile test, carried out in the rolling direction, at room temperature and for a strain rate of the order of $0.001\,s^{-1}$. $\bar{\sigma}$ is the equivalent stress and $\bar{\varepsilon}_p$ the equivalent plastic strain.

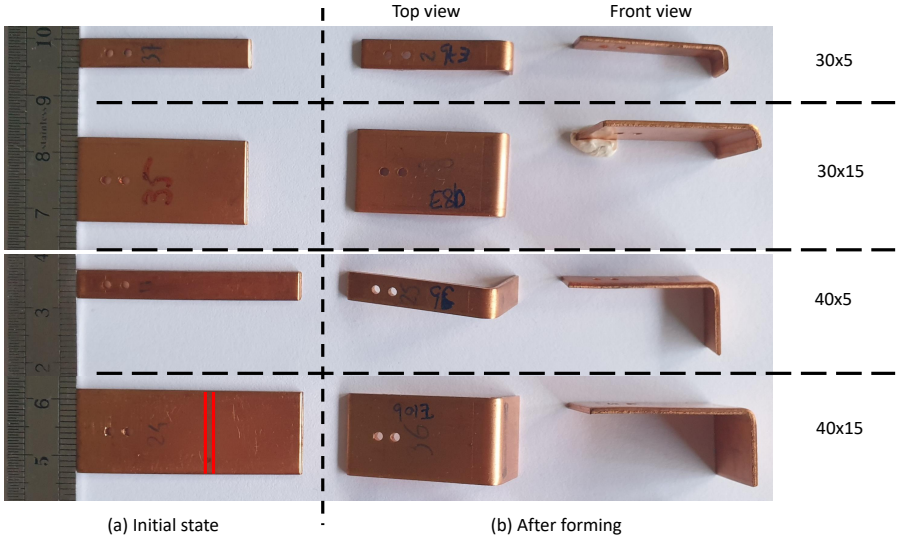

Fig. 3. Illustration of the different geometries of rectangular samples for Cu-DHP of thickness 1.2 mm before and after forming with the single stage bending tool. Shapes are very similar for Cu-ETP, although the sheet thickness is lower. The 2 red lines indicate the position of the blank holder. (dimensions in mm).

2.2 Experimental procedure

Specific experiments were carried out for the single stage bending process for rectangular samples, which are detailed here, whereas experimental results for the multi-stage process came from the industrial production.

2.2.1 Single stage bending

The geometries of the samples are chosen so as to change the length (30 mm or 40 mm) and the width (5 mm or 15 mm). The samples are cut from the copper strip by wire electrical discharge machining. Five repeatability tests are performed for each sample geometry. Figure 3 illustrates the 4 geometries as well as the final deformed shapes.

The single stage bending tool is shown in Figure 4. It includes a mobile upper part (upper block, punch holder, punch and stripper) and a fixed lower part (lower block, die holder and die). It has an upper block on which the punch is fixed by means of a punch holder plate. The stripper (or blank holder) allows to apply a clamping force on the sheet metal by means of springs during the bending

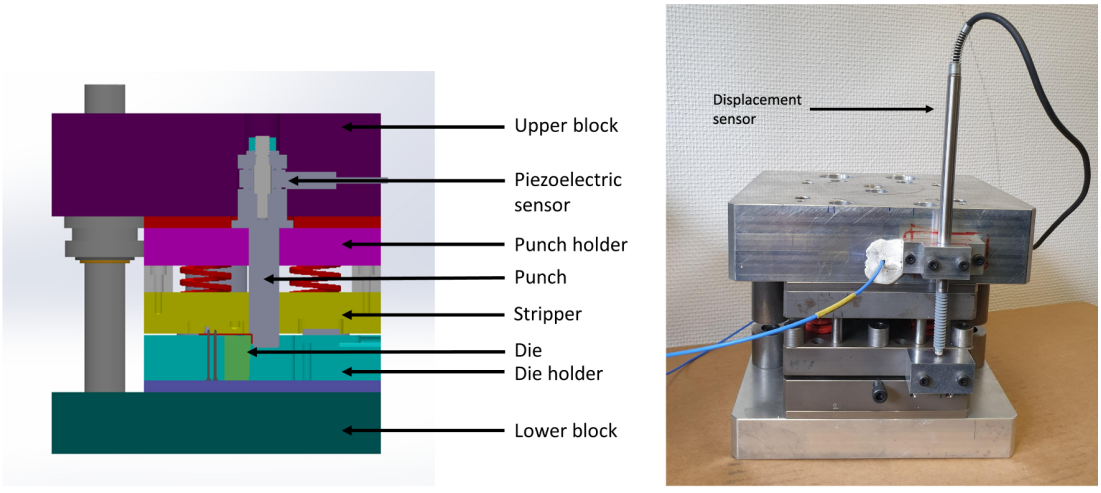

(a) (b)

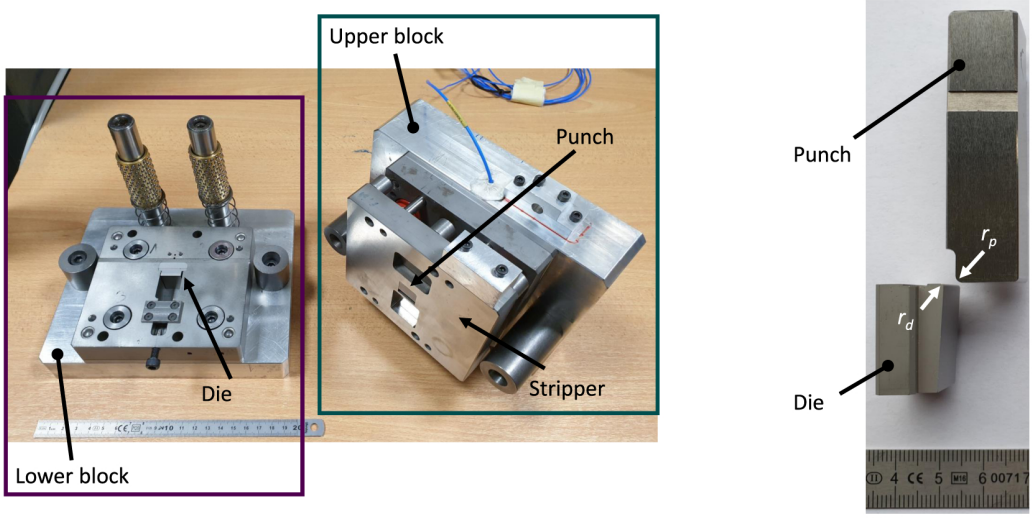

(c)

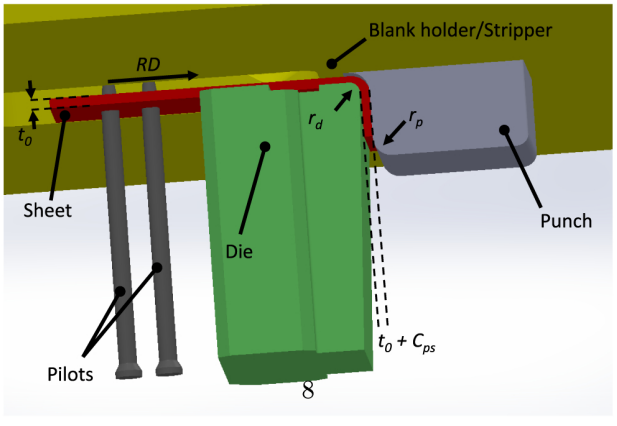

(d)

Fig. 4. (a) Cross-sectional view of the single stage bending tool; (b) Tool; (c) Upper and lower blocks of the bending prototype as well as the useful parts, such as the stripper, the punch and the die, used for the bending of sheets with a nominal thickness of 0.8 mm; (d) Schematic of the tools used for bending and their dimensions. For a sheet thickness of 0.8 mm, $r_d = 0.8$ mm, $r_p = 1.5$ mm, $C_{ps} = 3$ µm.

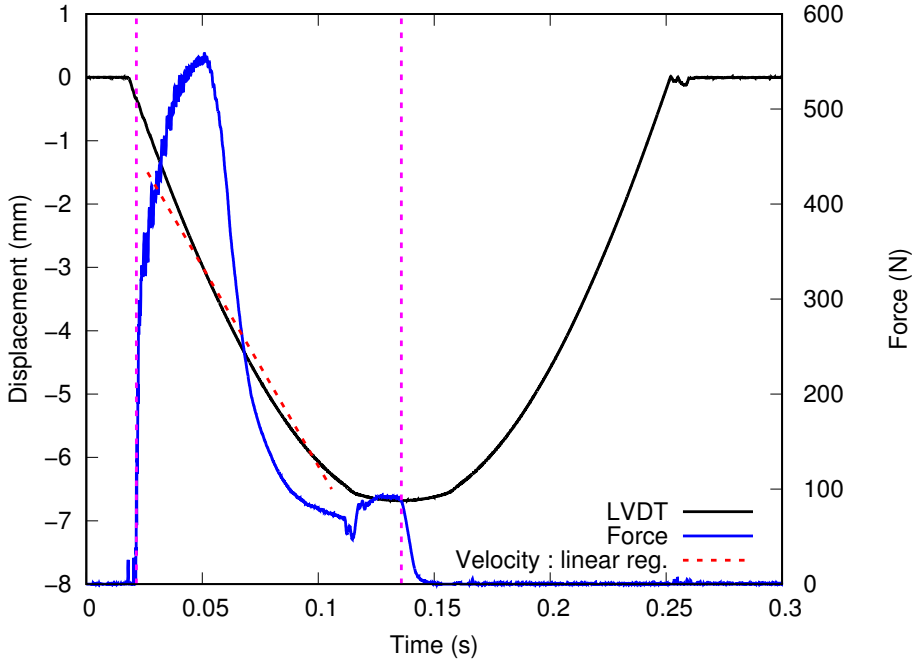

Fig. 5. Punch kinematics: displacement curve of the LVDT sensor as a function of time, the effective stroke of the punch is delimited by the two vertical lines.

process. The contact area between the stripper and the sheet metal is located in the area before the die radius. The blank holder clamps the sample over its entire width and over a length of 2 mm. The die holder containing the die is attached to the lower block. The sample is positioned on the die by means of two positioning pilots. The vertical movement of the upper block causes the sheet to be clamped between the stripper and the die before the sample is bent by the movement of the punch. Figure 4c shows images of the lower and upper blocks as well as the useful parts such as the stripper, punch, and die. The bending tool has a punch and a die which are characterized by die (r_d) and punch (r_p) radii. The gap between the punch and the sheet is noted C_{ps}; it corresponds to the distance between the die and the punch minus the initial sheet thickness. The schematic in Figure 4 illustrates the tools used for bending and their dimensions.

Tool instrumentation

The tests are conducted with a REMIREMONT mechanical press with a capacity of 1000 kN, located in an industrial workshop. The bending force is measured with a piezoelectric sensor (HBM CFW 50 kN). The force sensor is positioned above the punch so that the force on the punch is transmitted to the sensor through a spacer interposed between the base of the punch and the sensor (Fig. 4a). The sensitivity of a piezoelectric sensor depends on the set-up in which the sensor is in service. The error of measurement in force is ±0.5% (percentage of reading), it corresponds to the error of measurement of the load cell of 5 kN used to calibrate the sensor up to 1 kN. The displacement of the punch is measured indirectly by measuring the displacement of the stripper with a LVDT displacement sensor (Solartron AX/10/S). The acquisition is done with an HBM QuantumX MX840A at a sampling rate of 19.2 kHz. Figure 4b illustrates the instrumentation used.

Testing conditions

As the single stage bending tool can only produce one part at a time and the positioning of a sample and its removal from the tool are done manually, the mechanical press was used in manual control, with an imposed stroke of 30 mm to the mobile part of the press (or ram) and hence to the upper part of the tool. The vertical movement of the ram makes the tool close and open. The displacement sensor measurement is used to estimate the actual speed of the punch during bending.

Figure 5 illustrates the kinematics of the stripper and indirectly of the punch during a cycle. The displacement sensor registers a displacement when the springs begin to compress, which also corresponds to the beginning of the punch movement just before the start of the bending test. The press ram continues to move down to the bottom dead center position of the press. At this position the tool is completely closed, this is the end of the punch stroke. After the bottom dead center, the rise of the ram causes the opening of the tool. By calculating the slope of the curve during the descent of the punch, the actual speed of the punch is 63 mm/s. The slope is calculated for a displacement between −1.5 and 6.5 mm from a linear regression as shown in Figure 5. The effective displacement of the punch is defined from the superposition of the force and displacement signals as a function of time (Fig. 5), it corresponds to the relative displacement between the time instant when the load sensor starts to

register a signal and the bottom dead center which is the time instant before the inversion of the movement of the punch, which results in a decrease of the load. The effective displacement for bending the sample depends slightly on the experiment, in-between 6.27 mm and 6.34 mm.

Due to the technology of progressive tool, the blank holder force F_{bh} applied by the stripper during the bending process has a linear evolution in time which depends on the length of the compressed springs and indirectly on the punch displacement. The evolution of the blank holder force is measured experimentally from specific tests without sample, on a hydraulic machine. For a punch displacement ranging from 0 to 7 mm, the clamping force varies linearly from 1760 to 8064 N. In reality, it is the force on the springs that is measured, which gives a spring stiffness of approximately 900 N/mm to be compared to the value of 750 N/mm given by the supplier.

Springback angle measurement

The study of springback after the bending test is done through the measurement of the interior angle of the sample. The 3D scans of the parts are made with a KEYENCE VHX-7000 digital microscope equipped with a VH-Z20R lens for a magnification of 100 as shown in Figure 6a. The parts are scanned over an area corresponding to the width of the sample (5 or 15 mm) multiplied by a length ranging from 5.7 to 7.7 mm.

Once the scan is done, profiles are extracted along 5 regularly spaced lines as shown in Figure 6b. Figure 6c shows a profile from which linear regressions are made on both sides of the bent area. It also illustrates the sensitivity of the angle calculation to the intervals used for the linear regression. Depending on the intervals chosen, the angle can vary by 0.3°. The angle is calculated from the slopes of the straight lines using the formula $Angle = \arctan\left(\left|\frac{m_1 - m_2}{1 + m_1 m_2}\right|\right)$, in radians where m_i is the slope resulting from linear regression (Fig. 6c). By a propagation of uncertainties calculation, the accuracy of the springback angle measurement is estimated to be ±0.1°. Finally, an average is made from the 5 measurements for each sample. For each geometry, measurements are made for 3 samples to obtain a mean value and its standard deviation.

Strain field measurement

Measurements of the local strain field were performed to have an information on the strain state as well as the magnitude of the strain in the bent area. These measurements are made on the geometry 40×15 in Cu-ETP with three repeatability tests. Stereo image correlation system (Aramis 3D) is used for the measurement of the strain field on the sample surface located in the area of the external bending radius. As the bending tool is closed, it is not possible to follow the evolution of the strain field during the test, only the field at the end of the test after springback is measured. For this, a support was designed to fix the position of the sample in space for image correlation. Thereafter, the measurement of the strain field is made

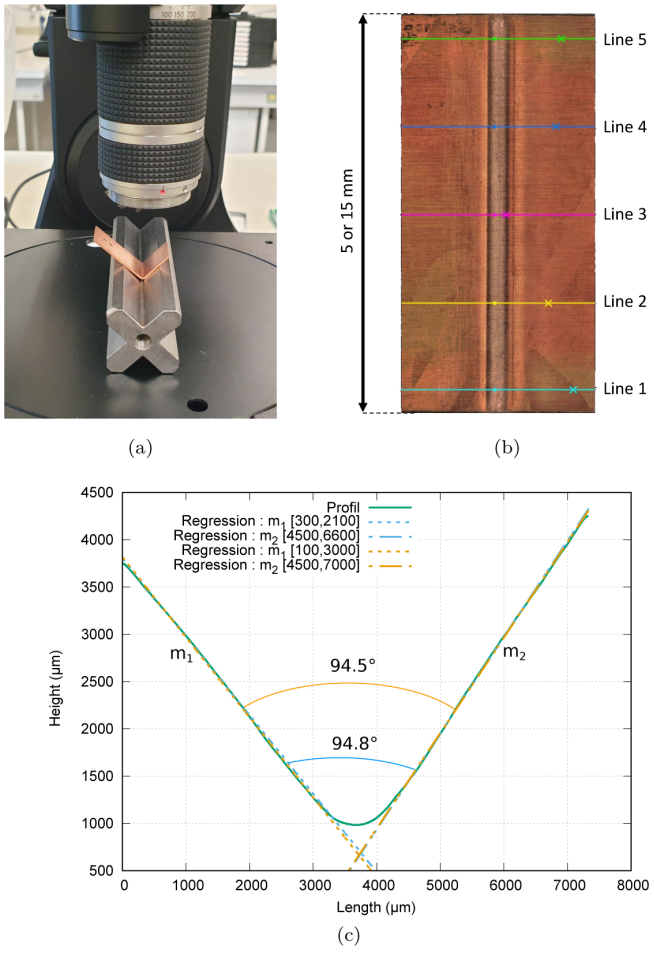

Fig. 6. (a) Illustration of a 3D scan of a part performed with a KEYENCE VHX-7000 digital microscope equipped with a VH-Z20R objective at a magnification of 100; (b) Interior scan of the part and positioning of the lines allowing the extraction of the profiles; (c) Illustration of the angle calculation methodology from a part profile and the sensitivity to the choice of regression intervals on both sides of the bending radius ($[300, 2100];[4500, 6600]$ and $[100, 3000];[4500, 7700]$, intervals in µm), the long edge of the sample is located on the left side of the profile. m_1 and m_2 stand for the slopes of the profile.

from images taken before and after bending. The strain values could be evaluated in the form of major/minor strain diagrams. The measurement points are taken in the area between the contact zone of the blank holder and the end of the bending radius. This zone corresponds to an area of approximately 2.5 mm × 15 mm as illustrated in Figure 7.

The configuration of the image stereo-correlation system (Aramis 3D), as well as the analysis parameters used to calculate the strain components, are presented in Appendix A.

Figures 7a and 7b show, respectively, the major ε_1 and minor ε_2 strain field measured on a sample in Cu-ETP (45°/RD). The major strain field shows a localization zone located in the outer radius of bending. This is an area subject to tension where the major strain can reach 0.409. The analysis of the minor strain field shows that

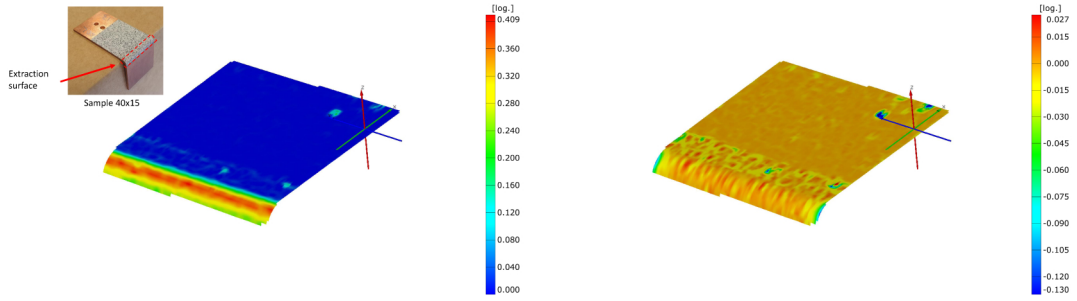

(a) Major strain (b) Minor strain

Fig. 7. Major (a) and minor (b) strain fields obtained with Aramis 3D on a sample of geometry 40×15 in Cu-ETP in the 45°/RD direction (an interpolation is used to fill in the areas of the mesh not calculated) and extraction surfaces (red delimited area) of the strain points.

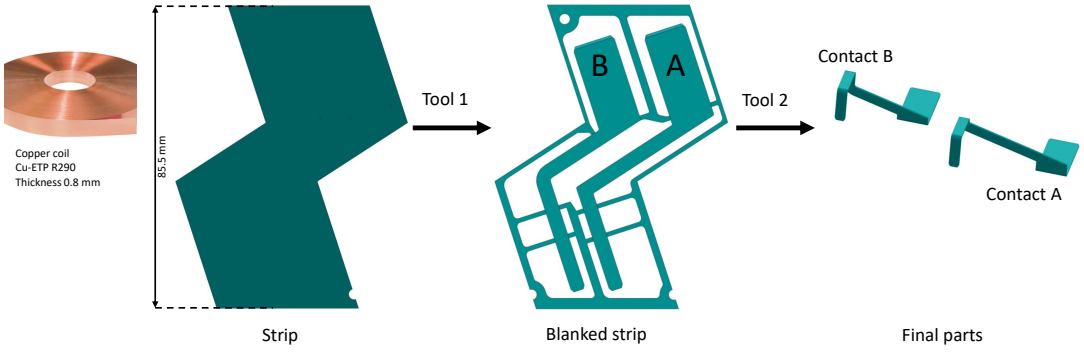

Fig. 8. Diagram of the manufacturing process for **contacts A** and **B**. The parts are obtained by passing the strip through the **tool 1** (blanking) and then the **tool 2** (bending and blanking/shearing). The 2 contacts differ only in the length of the arm between the two ends. Only **contacts B** is considered for the rest of the study.

the central area tends to deform in plane strain with a strain value of almost zero. The minor strain at the bent edges can reach −0.13. The area corresponding to the edge tends to deform according to a uniaxial tensile strain state.

2.2.2 Multi-stage bending

The electrical contact is obtained following blanking operations followed by bending operations. During this process, as shown in Figure 8, the copper strip goes through a progressive blanking tool (tool 1), to obtain a blanked strip which corresponds to the blanked part held by the skeleton of the strip. This first tool is not considered in this study. The blanked strip then goes through a second progressive bending tool (tool 2) to produce the final part. As the strip progresses through the tool, the parts will be detached from the skeleton (cutting operations) to allow the bending. The last operation consists in extracting the deformed parts from the skeleton (shearing operations).

Figure 9 illustrates the different operations required to produce the contact with a production rate of 100 stroke/min (60 mm stroke). **Stage 1** consists of the bending of **area a**. **Stage 2** corresponds to 2 forming operations performed simultaneously. To simplify model data settings, this stage is split into 2 sub-stages: **stage 2-1** corresponds to a calibration of **area a** using a cam slider system and a rotary punch. During its descent, the punch will slide on the cam slider and will undergo a rotation in addition to the vertical translation. The springback after the first bending leads to a higher angle and the calibration operation leads to an overbending in order to compensate the springback and thus tend to a 90° bending angle as defined by the part specifications. Subsequently, **area b** is bent during **stage 2-2**. It should be noted that unlike in the case of **stage 1**, the bending of **stage 2-2** is performed in the opposite direction upwards, the positions of the die and the punch are reversed (the die is located in the punch holder and the punch in the die holder). It is the vertical movement of the part, held between the die and a blank holder, during the closing of the tool that will cause the bending. The last stage is the bending of **area c** which is preceded by the blanking of **attachment points 1** (Fig. 10). Finally, shearing operations at **attachment points 2** are used to extract the part from the strip. At the end of each bending stage, when the part is no longer constrained in the tools, the part can undergo springback which is taken into account in the numerical model.

The geometric dimensions of the final part are defined by product specifications. Bent part is defined by three bent areas corresponding to **angles a**, **b** and **c** (cf. Fig. 10). The target angle is 90° with a tolerance

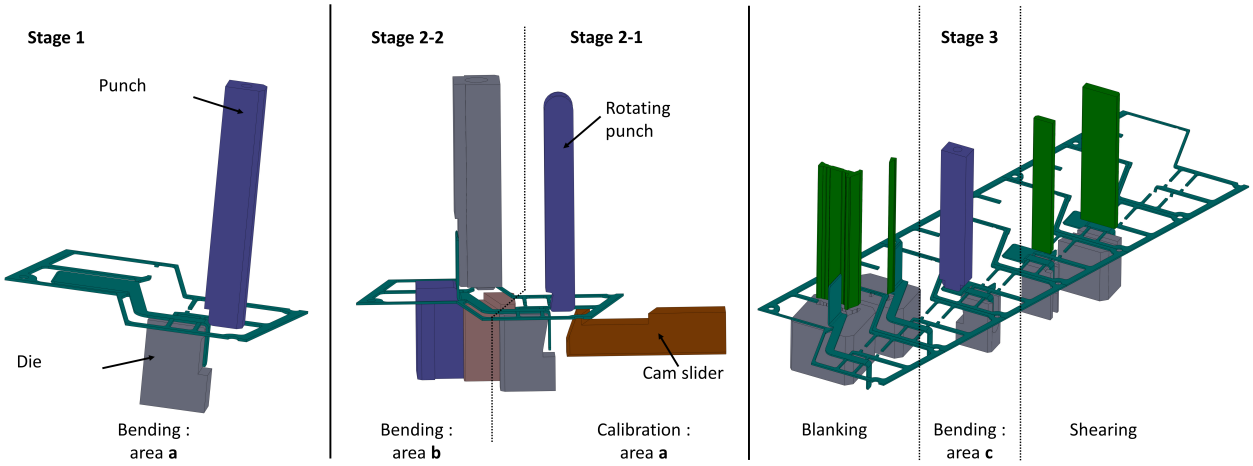

Fig. 9. Illustration of the different bending stages, blanking/shearing stages allowing the production of the electrical contact from the blanked strip, the blanking and shearing stages are modelled with boundary conditions.

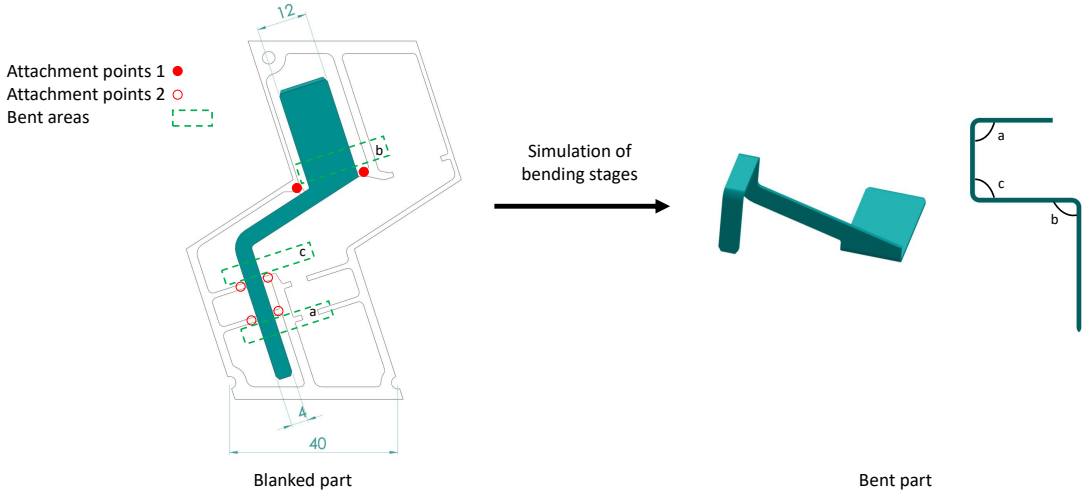

Fig. 10. Schematic of the manufacturing process of the electrical contact.

of ±2° for the **angles a** and **c** and ±3° for the **angle b**. A quality control sheet is used to monitor the process during production, and checks are carried out on the final geometry of the part at the end of the process. The **angles a** and **c** are checked using a profile projector, and the angle values are reported on the control sheet. From these measurements, it was possible to calculate average **angles a** and **c** and their standard deviations over 26 measurements. The **angle c** is checked using a jig; it is a qualitative check, hence the absence of measurements. The target angle values, along with experimental data in terms of mean angle, standard deviation and minimum and maximum angle values, are reported in Table 1.

2.3 Numerical simulation

2.3.1 Single stage bending model

The 3D model of the single stage bending process is performed with Abaqus/Standard, cf. Figure 11 for the 40×15 geometry. Actual sheet thickness of 0.792 mm is used for the comparison of experimental with numerical data, as a value averaged from the thicknesses measured on the samples tested during the test campaign. The final geometry is obtained following two successive calculation steps with an implicit resolution scheme. The first step corresponds to the forming operation, followed by a springback step.

The geometry of the tools (punch, die, blank holder) comes from the CAD model. The tool widths at the die and punch radii are 16 mm. The tools are described by rigid discrete surfaces. They are meshed with rigid discrete 3D quadrangular elements with 4 nodes (R3D4). The plane surfaces of the tools are meshed with an element size of 0.4 mm and the radii using a size corresponding to the radius value divided by 10. Only one half of the sample in the width is modelled because of the symmetry of the problem with respect to the width of the sample. The deformable blank is meshed with quadratic hexahedral type elements with 8 nodes and a reduced integration

Table 1. Values of the targeted angles by the specifications for **angles a**, **b** and **c**, as well as experimental data (mean angle, standard deviation, minimum and maximum angle values), the N/A character corresponds to not available data.

Angles	Theoretical	Experimental			
	Targeted angle	Mean angle	Standard deviation	Minimal angle	Maximal angle
a	90° ± 2°	89.36°	0.45°	89.00°	90.50°
b	90° ± 3°	N/A	N/A	N/A	N/A
c	90° ± 2°	89.82°	0.80°	88.00°	92.00°

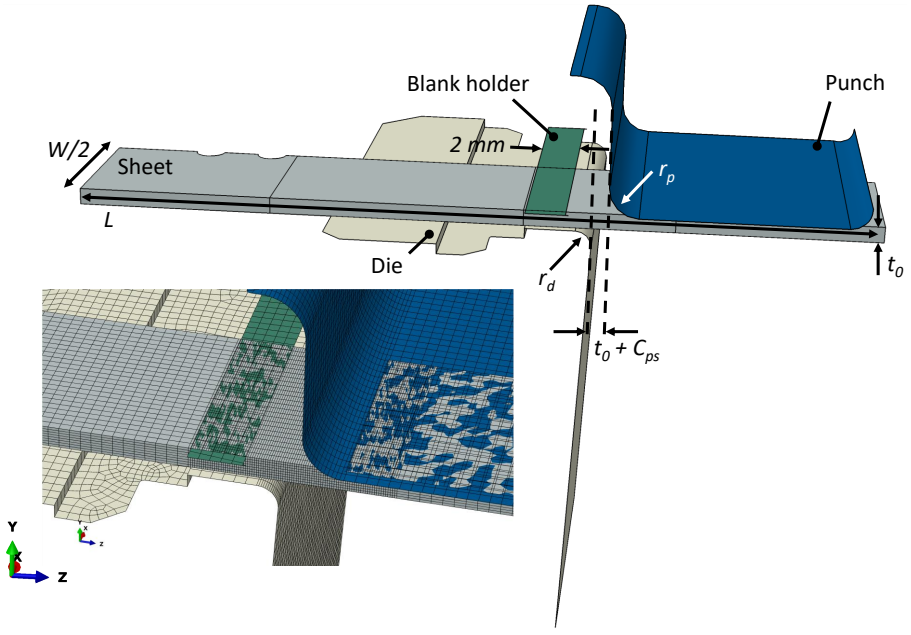

Fig. 11. Numerical single stage bending model for a sample geometry of length L and width W and tool geometries. Zoom: meshes of the deformable sample and rigid tools.

(C3D8R). A refined mesh is used in the deformed area where the element dimensions in the length and width are 0.08 and 0.3 mm. Eight layers of elements are used in the thickness. Outside of the refined areas, an overall mesh size of 0.4 mm is used. A mesh sensitivity analysis was performed: from 0.06 to 0.1 mm in the length, from 0.1 to 0.3 mm in the width and from 3 to 10 elements in the thickness. The values that offer a good compromise between calculation time and stability of the equivalent plastic strain and springback angle were used. These values are in agreement with previous works on the numerical simulation of bending, as presented in the introduction, with a number of layers of elements in the thickness of the sheet in the range of 4 to 16 layers.

The boundary conditions of the bending problem are described in Figure 12. All degrees of freedom of the die are blocked. To represent the conditions of the positioning of the sample by the pilots, the nodes of the contact surfaces with the pilots are left free to move in the direction normal to the sheet plane and blocked in the other directions. The blank holder force F_{bh} is applied according to a linear evolution that depends on the displacement of the punch. To apply this force, only the degree of freedom in the direction normal to the plane of the sheet is left free. The punch is controlled in displacement noted d. For the purposes of the sensitivity study of the model, a maximum theoretical displacement of 7 mm is used, this value will be adjusted with the experimental displacement value, which depends on the tested configuration.

For the springback step, the nodes of the pilot contact surfaces with the sample are locked in displacement to avoid rigid body movement of the sample. And the contact between the tools and the specimen is disabled. The different strategies to simulate springback, i.e., removal of contacts or by inverse tool movement, was not analysed in this study.

Friction model and friction coefficient calibration

The contact between the rigid tools and the deformable sheet metal is modelled by Coulomb's law. The model for the 40×15 geometry is used to study the sensitivity to friction between the punch and the sheet metal. A given punch/sheet metal clearance is fixed by CAD model of the tool, corresponding to 11 µm. During the simulation of the bending process, the contact of the sheet with the blank holder, the die and the punch is taken into account. There is no influence of the sheet metal contact with the die and the blank holder, and therefore the sensitivity analysis

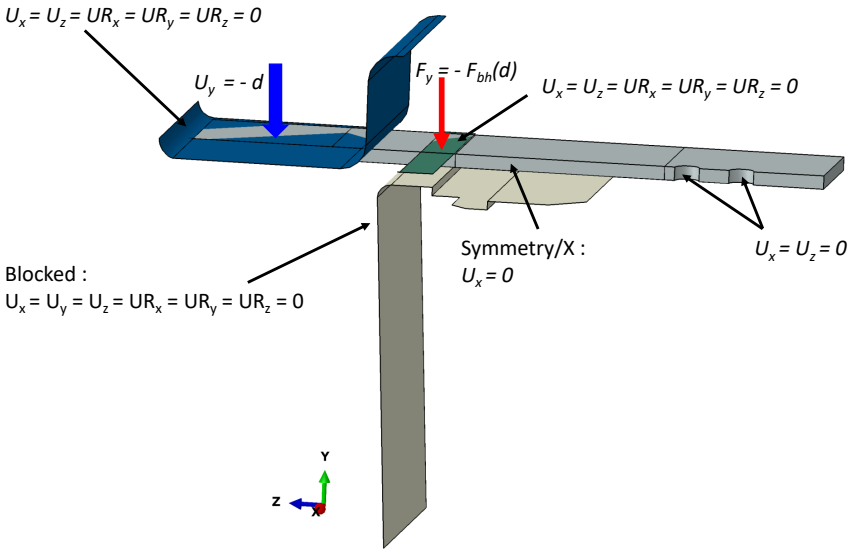

Fig. 12. Boundary conditions applied to the bending step.

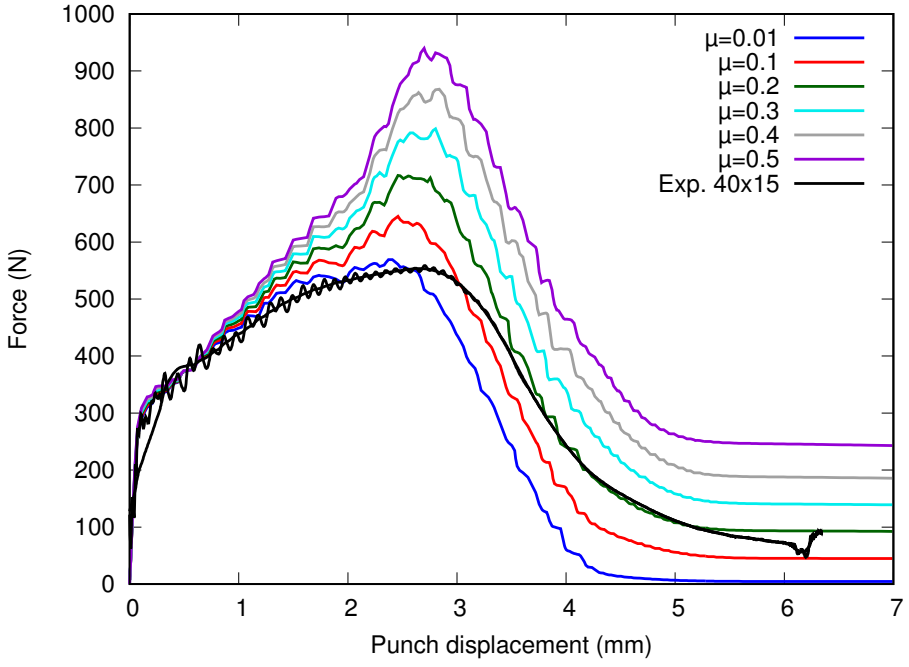

Fig. 13. Influence of the friction coefficient μ on the force evolution. Comparison with an experimental result obtained on the material Cu-ETP with the 40×15 geometry.

is focused on the sheet metal/punch contact. Coulomb's friction coefficient μ values ranging from 0.01 to 0.5 for the sheet/punch contact were tested in simulation. The friction coefficient is fixed at 0.05 between the sheet and the other tools.

The punch force-displacement curves in Figure 13 highlight the fact that bending requires a higher level of load as Coulomb's coefficient increases. The effect of the friction coefficient on the force curve is not very significant until a displacement of the punch of about 0.52 mm, which corresponds to an inflection point on the curve. This point characterizes the beginning of the bending of the sheet by the action of the punch radius. From this point, the increase of the friction coefficient has for effect an increase of the slope of the evolution of the force to reach more important values of the maximum force F_{max}. From F_{max}, the force drops to reach a constant value at the end of the bending, which depends on the friction coefficient.

The simulation analysis shows that up to about 4 mm of punch displacement, the bending is achieved with the punch radius. The remaining stroke between 4 and 7 mm corresponds to the phase of the bending operation where the sheet is fully bent and contact is essentially made

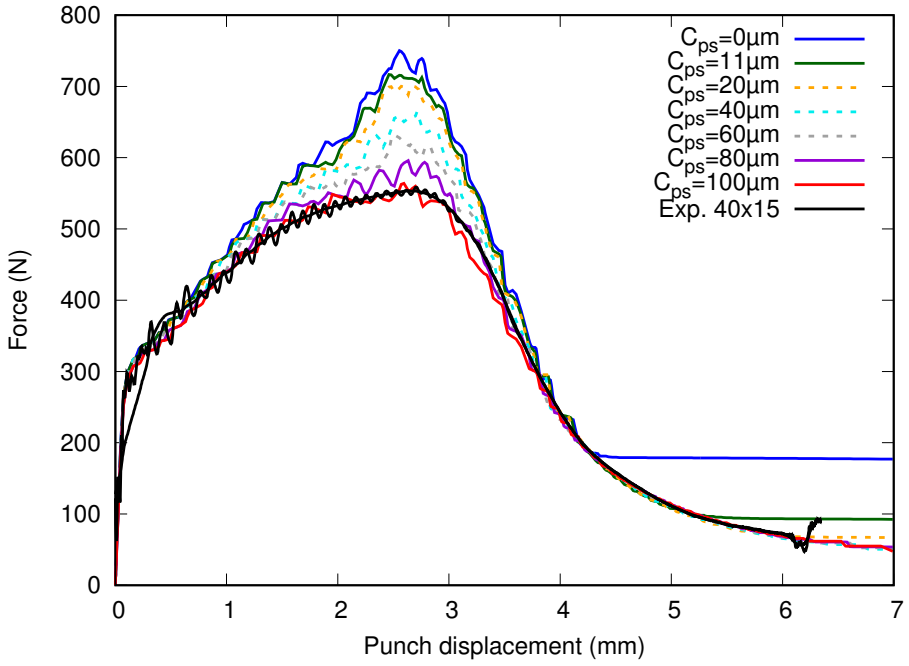

Fig. 14. Influence of the clearance C_{ps} on the force curve compared with a experimental curve obtained on the material Cu-ETP with the 40×15 geometry.

along the two flat surfaces of the vertical face of the punch and the outer surface of the sheet. This step can be compared to a tribology test. For this reason, during the sensitivity analysis, this part of the curve is used to set a friction coefficient based on the experimental data.

The comparison of the numerical force-displacement curves with an experimental one obtained on the material Cu-ETP with a 40×15 geometry is done in Figure 13. This comparison on the previously defined displacement interval shows that a friction coefficient of 0.2 gives a close description of the experiments. Therefore, this value is kept for the remaining part of the study. The load evolution with the punch displacement exhibit oscillations which magnitude depends on the mesh size, certainly stemming from the contact between the blank and the die in the bent area.

Punch/sheet clearance calibration

The model for the 40×15 geometry in Cu-ETP is used for the study of the sensitivity of the punch/sheet clearance, with values ranging from 0 to 100 µm; the clearance of 11 µm corresponds to the theoretical value defined in the CAD model.

The load evolution is presented in Figure 14. It shows that the influence of the clearance is mainly concentrated on the interval of the punch displacement going from 0.07 to 4 mm, a decrease of the clearance leads to a significant and rather abrupt of the maximum load F_{max}. Moreover, for low values (0, 11 and 20 µm), a zone with constant load appears close to the end of the bending. For a null clearance, the force becomes constant from a displacement of about 4.3 mm. During the process, a bending torque is required to form the sheet metal and the magnitude of the lever arm increases with the clearance increases, leading to a load decrease.

Figure 15 highlights further the dependance of the maximum load to the clearance. The continuous decrease is quasi-linear, especially for a clearance larger than 11 µm. The maximum force goes down from 750 to 564 N for respectively a zero clearance and a clearance of 100 µm, it decreases by 25%. This trend is similar to previously published results [28].

The clearance influences the maximum punch load and the load evolution close to this point, as well as the load level at the end of the process. Whereas the friction coefficient influences the breadth of the load evolution. Choosing a clearance value and a friction coefficient that lead to an overall correct description of the load evolution was done through a trial-and-error method, and these values give the best compromise.

The comparison with experimental values recorded on the material Cu-ETP for a 40×15 geometry is done in Figure 14. It shows that for a clearance of 100 µm, the simulation gives a good representation of the experimental curve. Therefore, a clearance between the punch and the sheet metal of (C_{ps} = 100 µm) is kept for the numerical calculations.

After the sensitivity analysis and the choice of some parameters for the single stage bending model, the next section presents the multi-stage bending model.

2.3.2 Multi-stage bending model

The approach consists in modelling the different bending stages allowing the forming of the contact as shown in Figure 10. The model is built from the CAD model of the blanked part [26,27]. The skeleton of the strip is

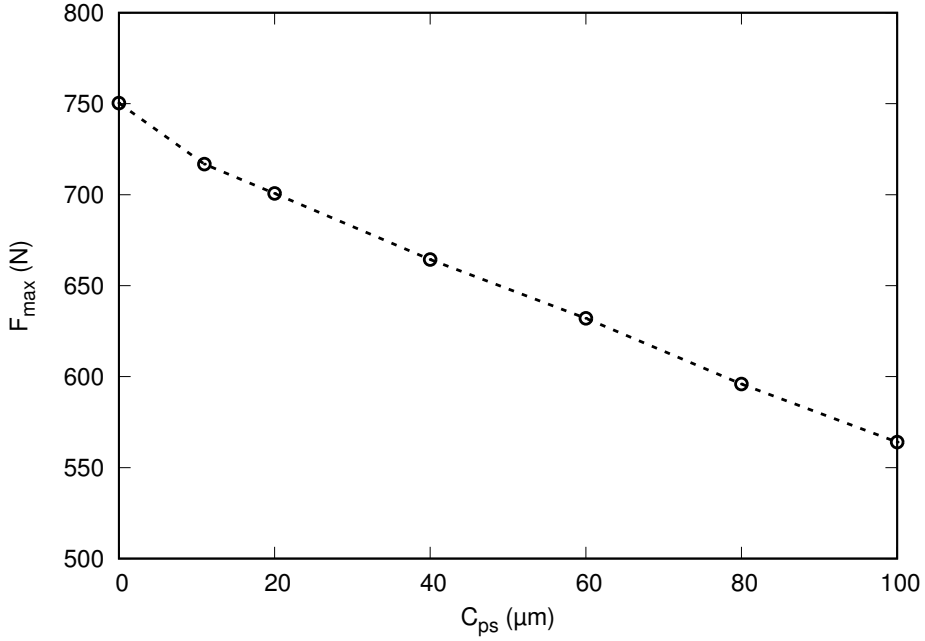

Fig. 15. Influence of the clearance C_{ps} on F_{max}.

Table 2. Geometries of the tools, clearance between the punch and the sheet given by CAD model and punch displacement d in absolute value.

Stages	W_d (mm)	W_p (mm)	r_d (mm)	r_p (mm)	C_{ps} (µm)	d (mm)
1	8	7.5	0.8	1.5	0	4.5
2-1	8	7.5	0.8	0.8	0	4.5
2-2	13	12.5	0.8	1	0	5
3	10	8	0.8	1.5	12	4

not modelled, the attachment points of the part with the skeleton are modelled by boundary conditions. This approach requires to neglect the influence of the blanking on the bending. Moreover, according to the know-how of the stampers, the sequence of the blanking operations is studied in order to avoid the twisting of the sheet and to ensure the flatness of the blanked part. Considering these assumptions, the blanking is neglected in a first approach with the use of the CAD model of the blanked part.

The 3D model of the multi-stage bending process of the electrical contact is based on the single stage bending model, i.e., the same copper behavior model, mesh parameters (Fig. 16b) and friction between the tools and the sheet are used.

The final geometry is obtained following six successive computational steps with an implicit resolution scheme. Each of the bending **stages 1**, **2** and **3** are followed by a springback simulation step. The geometries of the blanked part and the tools (punches, dies, blank holders and die holders) come from the CAD model provided by the industrial partner. The tools are designed for a theoretical sheet thickness of 0.8 mm. The positioning of the tools and indirectly the clearance between the punch and the sheet (C_{ps}) are imposed by the CAD model. It was shown in the previous section, through the comparison of the experimental and numerical evolution of the punch load, that the clearance set in the CAD model did not give a correct load prediction. However, in case of the multi-stage bending process, as no comparison with experimental values is possible, the clearance was kept equal to the one defined in the CAD model. The die (r_d) and punch (r_p) radii, as well as the tool widths at the die (W_d) and punch (W_p) radii and the clearance (C_{ps}) are defined in Figure 16a and in Table 2. The tools are wider than the blank widths.

The boundary conditions of the bending stages are defined in Table 3. The blank holder force is neglected in this model, it is kept at a fixed position during the bending. In the same way, all the degrees of freedom of the dies and die holders are fixed. The sheet is constrained by the attachment points with the skeleton, which prevent the part from moving in the plane of the sheet. The **attachment points 1** and **2** are therefore modelled by blocking the displacement of the nodes of the corresponding surfaces in the plane of the sheet. Only the displacement in the direction normal to the plane of the sheet is left free. In **stage 3**, the degrees of freedom of **attachment 1** are left free to model the blanking. The punches are controlled in displacement, which values are given in Table 2. In addition to a vertical displacement, the rotating punch of **stage 2-1** is controlled in rotation to model the action of the cam slider. Indeed, this action is

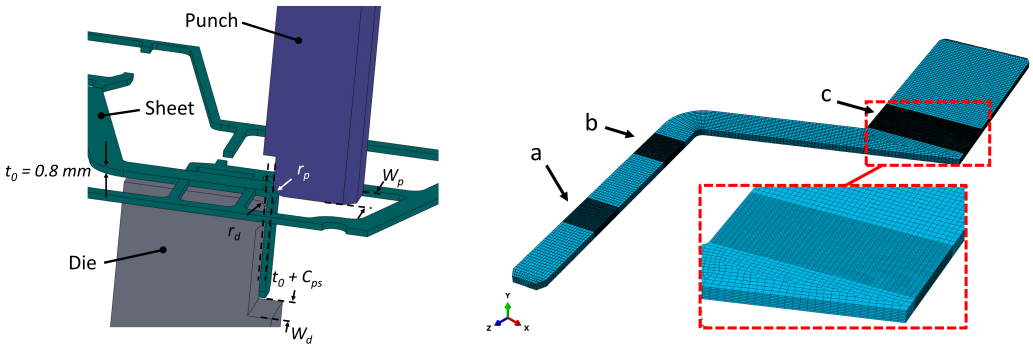

(a) (b)

Fig. 16. (a) Geometries of the tools; (b) Mesh of the part and its 3 bent areas, the mesh is composed of 63 912 elements for a total of 75 411 nodes.

Table 3. Boundary conditions of the bending stages. U_x, U_y, U_z (respectively UR_x, UR_y, UR_z) stand for the displacements (respectively rotations) of the node of coordinates x, y, z.

Geometries	Stages	Boundary conditions
Die Die holder Blank holder	1 ; 2-1 ; 2-2 ; 3	$U_x = U_y = U_z = UR_x = UR_y = UR_z = 0$
Punch	1 ; 2-2 ; 3 2-1	$U_x = U_z = UR_x = UR_y = UR_z = 0$; $U_y = d$ $U_x = U_z = UR_y = UR_z = 0$; $U_y = d$; $UR_x = \theta\,(d)$
Attachment point 1	1; 2-1; 2-2 3	$U_x = U_z = 0$ and U_y free U_x; U_y; U_z free
Attachment point 2	1; 2-1; 2-2; 3	$U_x = U_z = 0$ and U_y free

represented through boundary conditions, cf. Section 3.1 for a detailed description.

The simulation of the bending stages is followed by a springback calculation stage. During these calculation steps, the contact between the tools and the sheet is desactivated. The nodes of the **attachment points 1** and **2** are used to lock the sheet and to avoid a rigid body movement. For the final springback step, only the nodes on the surfaces of the **attachment points 2** are blocked, the nodes of the **attachment points 1** being free.

The computation time is 16 hours using 16 computational units with a computer equipped with two Intel(R) Xeon(R) Gold 6128 processors.

3 Results and discussion

This section is divided in 4 parts, related to the modelling of the cam slider and its role in controlling the springback, and then to the prediction of the bending load, of the deformed shape and strain prediction, and finally, of the springback.

3.1 Modelling of the cam slider action

The calibration operation comes after a bending operation in order to compensate the springback that occurs after the bending. This calibration stage is carried out with the help of a rotating punch and a cam slider system, which role is to apply a rotation to the punch, in addition to its vertical movement. The setting of the cam position is usually done by the operator when starting up the production line. Before each production run, the operator tests and adjusts the tool to ensure the conformity of the parts produced. This trial-and-error method can be costly in terms of time and material, and could be controlled more accurately. The action of the cam slider is modelled in this study through boundary conditions, to avoid modelling the punch as a deformable body and thus save computational time.

Representation of the movement of the rotating punch

Figure 17 shows the geometry of the cam slider and the rotating punch as defined by the CAD model. The cam is defined by an angle of 70° with the horizontal. The radius of the punch r_c in contact with the cam slider is 2 mm. In its initial position, the cam slider is located at a distance of 0.69 mm from the punch. The setting of the cam slider position is defined by X with $X = 0$ mm in the initial position as shown in Figure 17c.

The movement of the cam can be decomposed in 2 phases (Fig. 17c). In the first phase, the attachment of the punch in the tool is considered sufficiently rigid for the punch to move vertically until the contact with the cam slider. Once the contact occurs, the punch continues the vertical movement, to which is added a rotation. The magnitude of this rotation is a function of the vertical displacement and is defined in a local frame related to the punch, cf. Figure 17b. The upper end of the punch can be

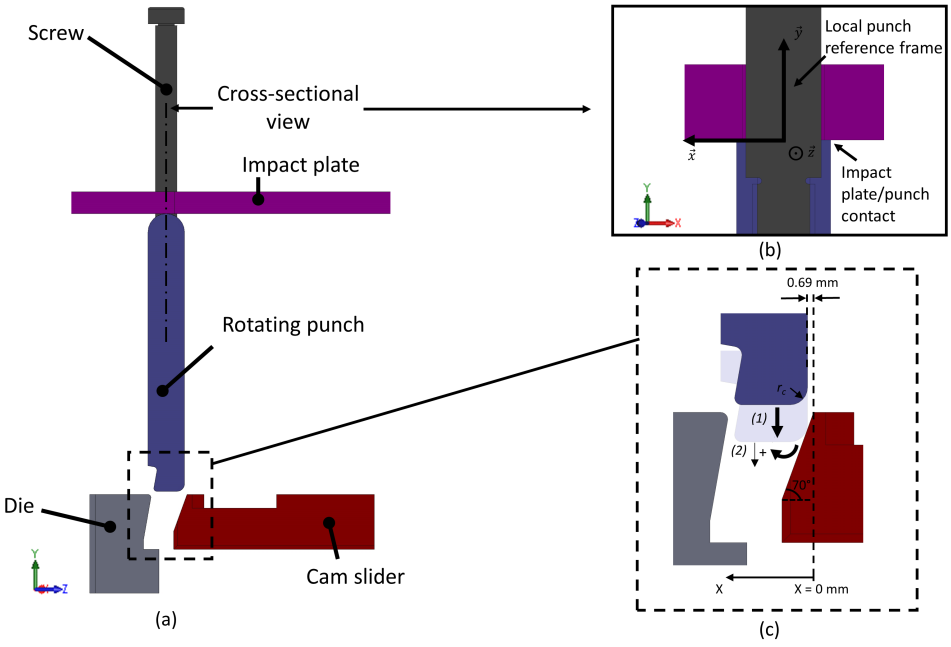

Fig. 17. (a) Illustration of the cam slider and rotating punch system and the geometrical parameters, radius of the punch (r_c) in contact with the cam slider, angle of inclination of the cam slider, distance of the cam from the rotating punch; (b) Cross-sectional view of the contact between the impact plate and the punch allows the definition of a local reference frame; (c) Decomposition of the punch movement.

considered as a cylinder and the impact plate to a plane. The contact is made along a line (straight line contact) around which the punch rotates, which defines the direction $\vec{x}$ of the local reference frame. The origin is defined as the intersection between the center of the screw fixing the punch and the $\vec{x}$ axis. $\vec{y}$ is the vertical translation direction of the punch.

A 3D elasticity model of the interaction between the cam slider and the rotating punch is developed in Abaqus within an implicit frame and used to predict the rotation as a function of the cam slider position setting. The predicted kinematics can be used as input to the **stage 2-1** of the bending model. The evolution of the rotation angle of the punch UR_x for several positions of the cam slider (X equal to 0, 0.05, 0.175, 0.35, 0.525 and 0.69 mm) is almost linear. The angle UR_x corresponds to the angle obtained at the end of the punch stroke. For a cam slider position ranging from 0 to 0.69 mm, the rotation angle varies from 0.0008 rad (0.046°) to 0.0116 rad (0.664°).

Application to the calibration stage (2-1)

The boundary conditions in displacement (U_y) and in rotation (UR_x) for 3 positions of the cam (X equal to 0, 0.05, and 0.175 mm) are given in Figure 18 for a computation time of 1 s. To analyse the influence of the cam action, a configuration without cam is also modelled by constraining the rotation UR_x, so that the punch keeps only a degree of freedom in displacement U_y.

The **angle a** is obtained after two successive operations of bending and calibration. The value of the targeted angle by the specifications is 90° with a tolerance of ±2° as illustrated in Figure 19. This graph also shows the value of the angle before calibration which is 91.60°. For the configuration without the cam slider, there is a negligible evolution of the angle, from 91.60° to 91.44°, before and after calibration. The evolution becomes significant with the cam slider. The angle goes down from 90.05° to 83.19° for a cam position ranging from 0 to 0.175 mm. The evolution of the calibration angle with the displacement of the cam slider is quasi-linear, with a sensitivity of the cam position on the calibration angle that is equal to 39.44°/mm. The angle tends to reduce as the cam advances, as illustrated by the deformed shapes of the different configurations with and without cam slider obtained at the end of the calibration stage for a displacement of 4.5 mm (Fig. 20). The point corresponding to a cam slider position of 0.175 mm is outside the tolerance, this setting seems extreme. Generally speaking, the angles obtained before calibration, without the cam slider, and for cam positions of 0 and 0.05 mm are within tolerance. However, the use of a cam slider with an adapted setting shows that it is possible to improve the final geometry and to approach the criterion of geometrical tolerance defined by the specifications. A cam slider position at 0 mm gives an angle of 90.05° close to the targeted angle of 90° and this position is kept for the numerical model. These values are obtained for fixed input parameters in the numerical model concerning the material thickness and hardening law, and the lubrication.

3.2 Load prediction

This subsection focuses on the comparison of the experimental data with the numerical prediction for the different configurations with Cu-ETP.

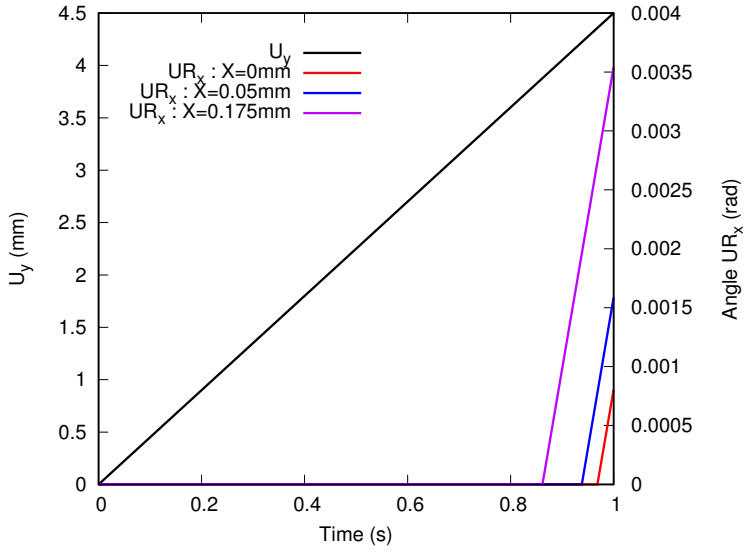

Fig. 18. Boundary conditions for **stage 2-1** in displacement (U_y) and in rotation (UR_x) for 3 positions of the cam slider (X equal to 0, 0.05, and 0.175 mm), for a computation time of 1 s.

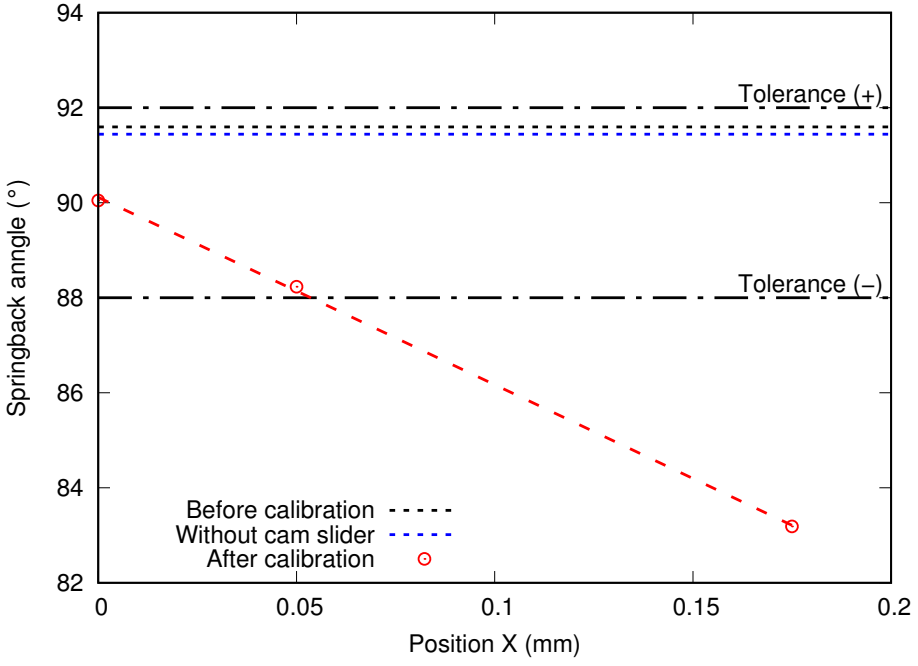

Fig. 19. Evolution of the calibration **angle a** with the cam slider position (X equal to 0, 0.05, and 0.175 mm), and the angle without cam slider and before calibration.

The measured force signals show oscillations that could be due to vibrational phenomena induced by the mechanical press as well as the speed of the bending test in a test time of about 0.12 s. Indeed, several authors have worked on modelling the dynamic behavior of high-speed screw press [37], high-speed servo press [38], high-speed mechanical press [39]. Moreover, the technology of fixing the punch with keys results in a degree of freedom in the direction of the punch movement, which could induce punch vibrations and oscillations on the force signal.

Thereafter, a representative curve for each geometry is presented, with a smoothed signal (moving average according to a regression of a polynomial of degree 3 on 50 to 150 measurement points). The values of the maximum force, F_{max}, are obtained from the smoothed signal. The graphs in Figure 21 shows the force-displacement curves measured for the different geometries bent in Cu-ETP in the rolling direction. Globally, the curve of the bending process is similar to the one presented in the literature [18]. It can be seen that, for a given sample length (30 or 40 mm), the curves are superimposed until the value of the

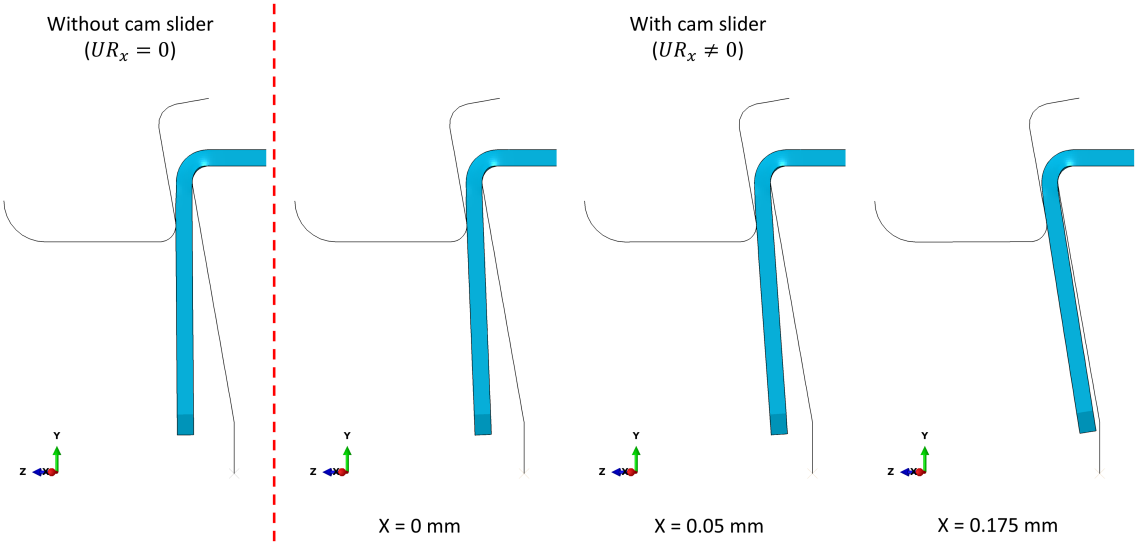

Fig. 20. Deformed shape of the different configurations with (X equal to 0, 0.05, and 0.175 mm) and without the cam obtained at the end of the calibration stage for a displacement of 4.5 mm.

maximum load. After reaching F_{max}, a difference in the load level can be noticed though the curve shape is similar. This difference may be due to a higher friction for the length 30 mm. Therefore, it seems that the length of the sample has no significant influence on the load evolution up to the maximum value.

As the width increases from 5 to 15 mm, the value of F_{max} also increases from about 202 to 554 N representing a factor of 2.7 which is close to the width ratio equal to 3. The level of the load as well as the value of F_{max} increase quasi-proportionally with the width of the sample. This quasi-proportionality is highlighted by plotting the load of the geometry 40×15 divided by the width ratio 3 in dotted line (Fig. 21b). As well as a higher friction when the load drops for the 5 mm width. The final load evolution is slightly dependent on the sample length, for both widths. As the length decreases, a higher friction coefficient is needed to obtain a better final load prediction. This could be obtained by introducing a pressure-dependent friction coefficient, provided that the contact pressure decreases with the sample length.

Figure 21a shows the superposition of experimental and numerical force curves for geometries of 15 mm width. The model parameters ($\mu = 0.2$, $C_{ps} = 100\,\mu m$) were identified from a test with the 40×15 geometry and give a good representation of the experimental curve. A good description of the experimental curve is also obtained for the 30×15 geometry up to a displacement of about 3.5 mm. For a displacement of 6 mm, the experimental and numerical load values are respectively 91 and 70 N, which is a relative deviation of −22.9% with respect to the experimental value. The tests for the 30×15 geometry show higher friction.

Similarly, Figure 21b shows the superposition of the experimental and numerical force curves for geometries of 5 mm width. The beginning of the experimental curves is very noisy compared to the curves obtained for a 15 mm width. The amplitude of the measured force being almost three times higher, this can act as a filter on the noise of the force signal. It appears that the prediction underestimates the force level at the elastic-plastic transition, which occurs earlier in the simulation. A shift of the position of the maximum load is also observed, this force is reached for a displacement of 2.91 and 2.57 mm on respectively the experimental curve (40×5) and numerical curve, that is to say a relative deviation of 11.7% with respect to the experimental value. This deviation is of 2.7% for the 40×15 geometry. Globally, the simulation tends to underestimate the force level compared to the experimental curve. Despite this, the model succeeds in predicting the trend of the curve up to F_{max} but a very important difference is observed after the maximum load and until the end of the test. These differences could come from the quality of the experimental curves obtained for the geometries of 5 mm width. Indeed, on the one hand, the load levels involved during bending remain relatively low, of the order of 200 N, and on the other hand, due to the technology of the tool which uses a floating punch system guided by a stripper that can generate noise. The absence of load drop is thought to come from an additional friction, not taken into account in the numerical model but existing in the experimental set-up. Several tests were carried out, with and without lubricant between the tools, and the drop was never observed for this geometry.

The histogram in Figure 22 shows the comparison of F_{max} values for the different geometries. The F_{max} values are obtained from an average of 4 to 5 tests except for the 40×15 geometry where only 2 to 3 tests could be post-treated. F_{max} values are obtained with standard deviations varying from 2.1 to 3.7 N. For a given sample width (5 or 15 mm), comparisons of F_{max} between the 30×5 and 40×5 geometries on the one hand and the 30×15 and 40×15 geometries on the other hand show that

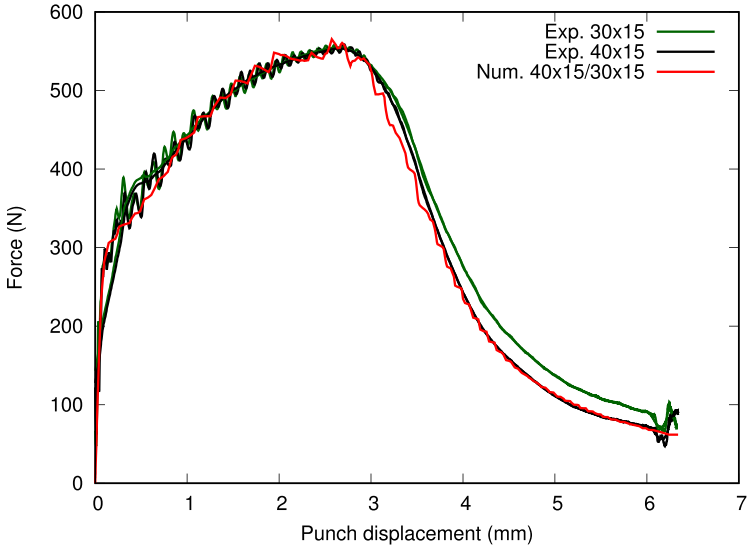

(a) 15 mm width

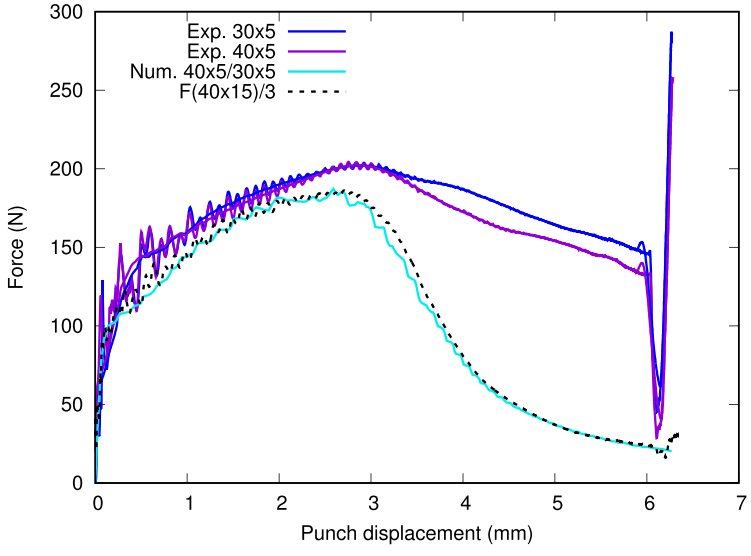

(b) 5 mm width

Fig. 21. Comparison of experimental and numerical force-displacement curves for the different geometries (40×15, 30×15, 40×5, 30×5) of the Cu-ETP sample for the rolling direction (0°/RD), in dotted line the experimental force curve of the geometry 40×15 divided by the width ratio equal to 3.

the load levels are similar. For example, the 30×15 geometry has an F_{max} value of 557 N and that of the 40×15 geometry is 552 N. Taking into account the variability of the test, the two geometries share a close force level. Thus, the change in bending length has no influence on F_{max}.

Figure 22 shows also the experimental-numerical comparison of F_{max} value for the different geometries tested. For the geometry 40×15, the numerical F_{max} value is 565 N, the experimental value is 552 N which is a relative deviation of 2.5% with respect to the experimental values. Similarly, the 30×15 geometry has experimental and numerical F_{max} values of respectively, 557 and 565 N which is a relative deviation of 1.5% with respect to the experiment. For 5 mm width geometries, the numerical F_{max} value is 187 N and the experimental values are 200 (30×5) and 187 N (40×5), that is respectively a relative deviation of −6.5 and −6.7% with respect to the experimental values. Finally, the models for 15 mm width tend to overestimate F_{max} value and underestimate it for 5 mm width. The absolute relative deviation for the prediction of F_{max} is between 1.5 and 7.6% for the different geometries tested, therefore the numerical model gives a satisfactory estimation of the maximum force in an industrial scope.

Comparison of single and multi-stage models

Figure 23 shows a comparison of the prediction of the load per unit width for **stage 1** with the one for the

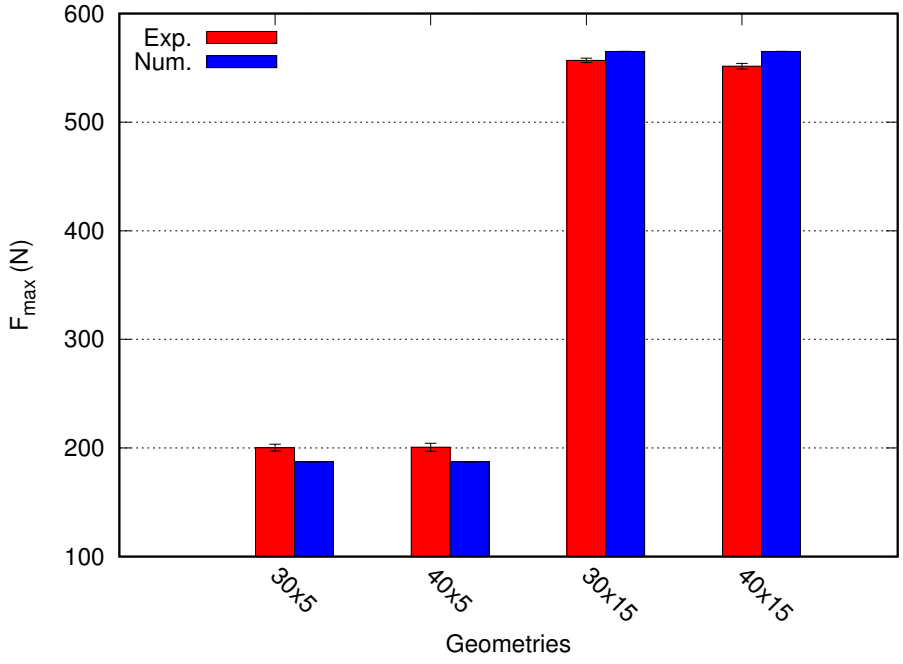

Fig. 22. Comparison of experimental and numerical F_{max} values for the different geometries tested in Cu-ETP in the rolling direction (0°/RD).

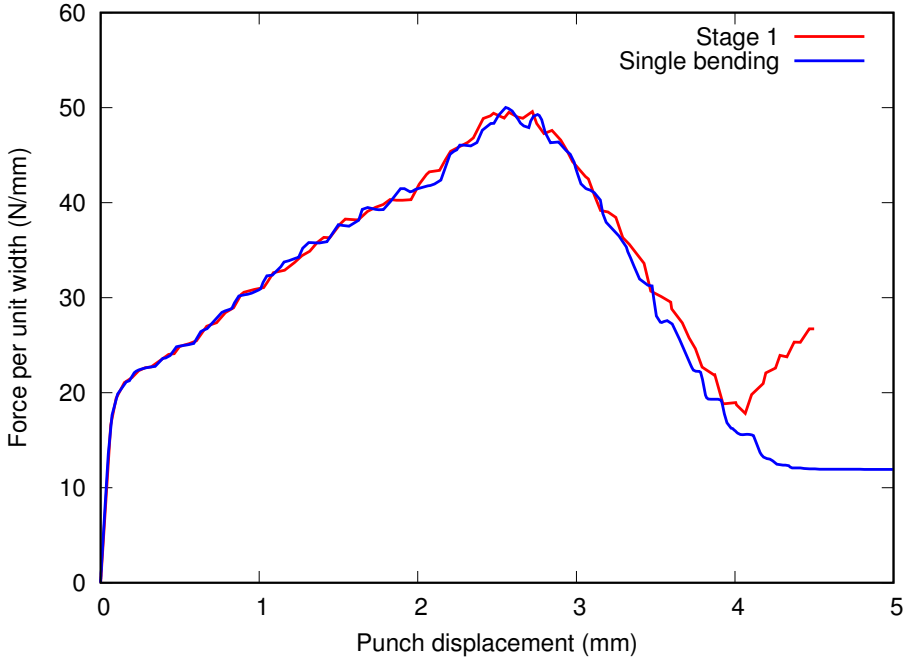

Fig. 23. Comparison of the force curve per unit width of the **stage 1** with that of the single stage bending model (rectangular geometry 40×15×0.8; thickness $t = 0.792$ mm; friction $\mu = 0.2$; clearance $C_{ps} = 0\,\mu$m).

single stage bending (rectangular geometry 40×15×0.8). These two curves share identical numerical parameters, the friction coefficient is 0.2 and the clearance C_{ps} is zero. The curves are almost merged up to a displacement of about 4.07 mm, the single stage bending model captures the maximum force of the multi-stage model. Starting from a displacement of 4.07 mm, the curves diverge, the curve of **stage 1** has an increasing force per unit of width while that of the single stage bending model continues to decrease to tend towards a constant value. This difference in behavior is induced by the shape of the die which is different, **stage 1** has a straight die and a tilted die (angle of 3° with the vertical) is used for single stage bending. The analysis of the numerical simulation shows that the

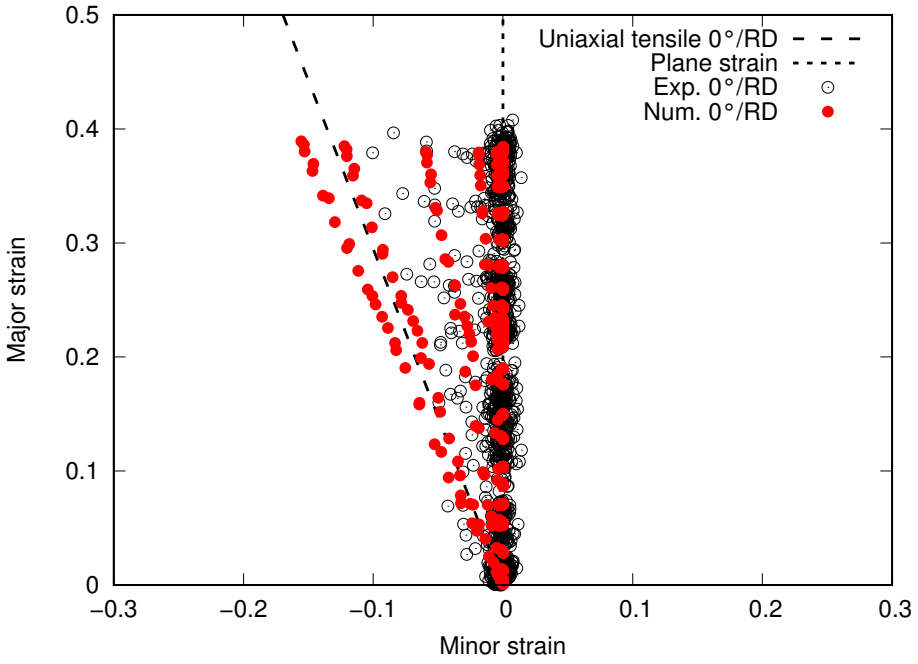

Fig. 24. Major/minor strain diagram obtained from the numerical model of the 40×15 geometry after springback and from measurement points made with Aramis 3D on Cu-ETP (0°/DL) samples.

use of a straight die generates a higher contact pressure between the sheet and the die and can be the cause of the force rise during the **stage 1**.

As a conclusion, the comparison of one stage of the multi-stage process with the single stage bending model shows that the single stage bending process is representative of the multi-stage process in terms of load.

3.3 Deformed shape and strain fields prediction

The numerical deformed shapes at the end of the bending step, for the same width (15 mm) and a length of either 30 mm or 40 mm, have been compared and no difference could be highlighted, which confirms that the sample length has no influence on the deformed shape.

Figure 24 shows the strain states on a diagram of major strain versus minor strain in the sheet plane. The plane strain state as well as the uniaxial tensile strain state taking into account the anisotropy are also represented, using the formula $\varepsilon_1 = -\left(\frac{1+r_0}{r_0}\right)\varepsilon_2$ with the anisotropy coefficient r_0. The diagram also shows the measurement points with DIC made on the 40×15 geometry in the rolling direction after springback, from a representative test. The sample is mainly deformed according to a plane strain state due to the density of points with ε_2 close to 0. Also, it appears points which move away from the plane strain state to approach a uniaxial tensile strain state. These points are measured near the bent edges (free edge) of the sample.

Figure 24 shows also the major/minor strain diagram obtained from the numerical model of the 40×15 geometry in Cu-ETP after springback. The data extraction area is equivalent to that used experimentally. In general, the central region of the half-sample has points in a plane tensile state with the minor strain close to 0. In this area, the major/minor strains reach 0.384 and −0.0001. Similarly, the transition from the central region to the edges of the bent width correlates with a uniaxial tensile strain state. The extreme point in uniaxial tension is located at the edge of the specimen and corresponds to major/minor strains of 0.389 and −0.155. The model is able to reproduce the major strain level of the central zone which is about 0.39. On the other hand, the model tends to overestimate the strain level of the points located in uniaxial tension. The comparison of the numerical and experimental strain fields was performed without considering the difference in the strain tensor calculation, over areas of different dimensions, fixed by the mesh size and the subset size respectively. This could explain the discrepancy on the strain level. It should be also noted that the deformation field obtained by DIC may be incomplete due to edge phenomena.

The comparison of the experimental and numerical geometry for the multi-stage bending is done in a qualitative way on Figure 25. The maximum value of the equivalent plastic strain on the external surface of the bending is obtained in the middle of the width. For each bent area, the values of $\bar{\varepsilon}^p$ evaluated at three nodes where $\bar{\varepsilon}^p$ is maximum is indicated. The values of $\bar{\varepsilon}^p$ vary from 0.409 to 0.435 over the different bent areas. These values are consistent with the single stage bending model of the rectangular samples where $\bar{\varepsilon}^p$ maximum varies from 0.435 to 0.437 (geometry 40×15 for C_{ps} ranging from 0 to 11 µm). Finally, the single stage bending model is representative of the multi-stage model in terms of the equivalent plastic strain.

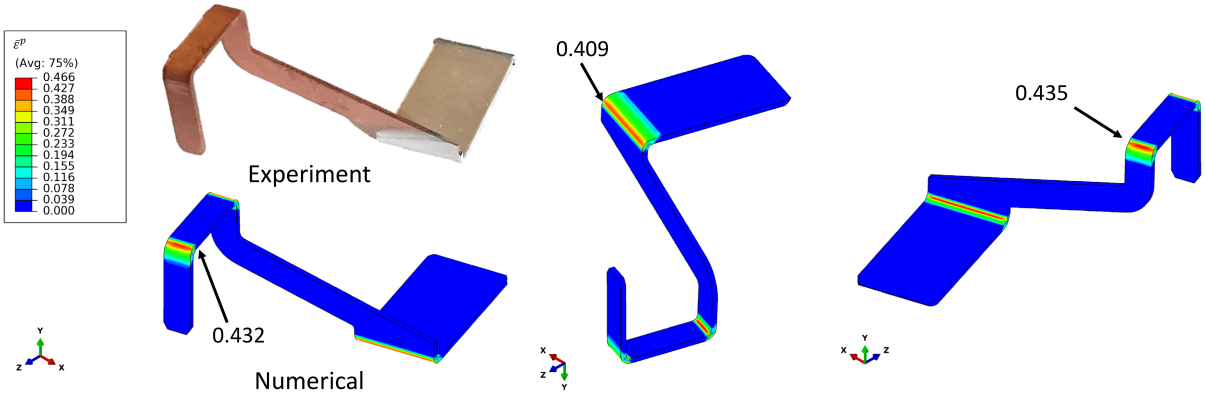

Fig. 25. Deformed shape of the different bent areas as well as the equivalent plastic strain iso-value $\bar{\varepsilon}^p$ for the final state. The maximum $\bar{\varepsilon}^p$ values are evaluated at a node located on the external radius, in the middle of the bent width.

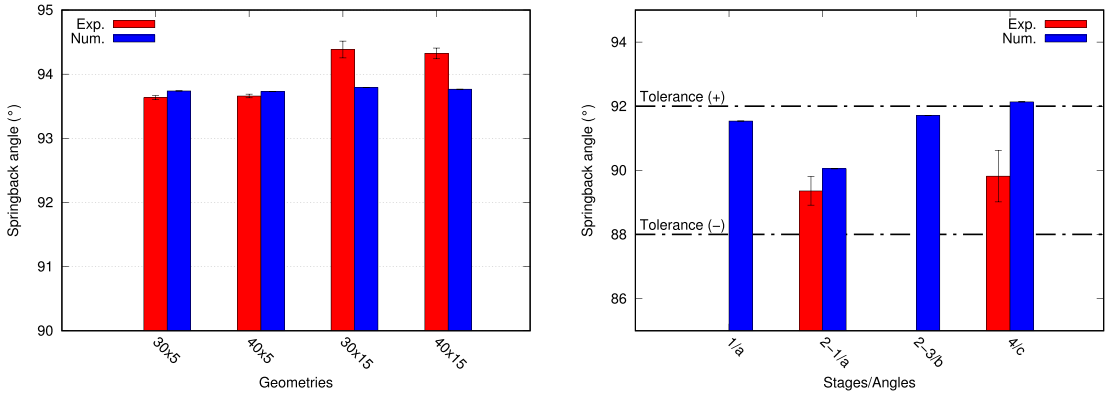

(a) Single stage (b) Multi-stage

Fig. 26. (a) Comparison of the experimental and numerical values of the springblack angle for the different geometries tested in Cu-ETP (thickness 0.8 mm) in the rolling direction (0°/RD); (b) Numerical values of the angles measured on the final geometry of the part obtained at the end of all the bending and springback stages, the value of the angle of **stage 1** corresponds to the one before calibration, and comparison with the available experimental data.

3.4 Springback prediction

Figure 26a shows the springback angle values measured after forming for the different geometries, with bending in the rolling direction. The standard deviation on the average angle value lies in the range from 0.03 to 0.13°. The maximum deviation between angle measurements is about 0.8°, the angle varies from 93.6 to 94.4° for the 30×5 and 30×15 geometries respectively. For a given sample length (30 or 40 mm), the angle increases by about 0.8° as the width increases from 5 to 15 mm. Thus, the average angle increases with the width of the sample, with length having little influence on the springback angle.

Figure 26a presents also the experimental-numerical comparison of the springback angle value for the different geometries tested. For the 15 mm width geometries, the numerical values of the angle are 93.79° and 93.77° respectively for geometries 30×15 and 40×15. Similarly, the experimental values are 94.4° and 93.8° for the 30×15 and 40×15 geometries, that is respectively a relative deviation of −0.6 and −0.03% with respect to the experimental values. For this width, the numerical simulation tends to underestimate the angle and thus the springback. For the 5 mm width geometries, the numerical values of the angle are 93.74° and 93.73° for respectively the geometries 30×5 and 40×5. The measured angles after tests are 93.6° and 93.7°, which gives relative deviations of 0.15 (30×5) and 0.03% (40×5) compared to the experimental values. The simulation tends to slightly overestimate the springback. In general, in the experiments, it was observed that the springback angle was larger for geometries of 15 mm. Changing from 40×5 to 40×15 geometry corresponds to an increase of 0.7% of the springback angle. This tendency is found in simulation but it is less marked, this increase of the angle is only of 0.04%. The increase of the experimental springback angle, when the sample width is increased, is not predicted. It may come from a friction contribution between the tools and responsible of the load evolution for the small width. It may also come from a limitation of the material mechanical model. Overall, the numerical models provide a good prediction of the angle after the springback step with an absolute relative deviation between 0.03 and 0.6%.

Considering the multi-stage bending, Figure 26b shows the numerical values of the angles measured on the final part geometry obtained after all the bending and

springback stages, except for **stage 1**, where the angle corresponds to the one before the calibration of **stage 2**. A comparison with available experimental data is also evidenced.

The numerical model highlights the role of the cam slider. The **angle a** changes from 91.54° to 90.05° following the calibration stage. The calibration operation leads to a closer value of the angle targeted by the specifications.

The experimental value of **angle a** is 89.36°. Furthermore, the numerical value of **angle a** at the end of **stage 2** is 90.05°. The numerical model overestimates the value of the **angle a** by 0.8% compared with the experimental value. Similarly, the experimental and numerical values of **angle c** are respectively 89.82° and 92.14°, representing an overestimation of 2.6% by the numerical model. This tendency of the numerical model to overestimate the angle after springback of a bent width of 4 mm is similar to the one found for rectangular geometries with comparable widths of 5 mm.

However, the springback angles predicted by the model are within process tolerances, except for **angle c**, which is on the high limit. Finally, the multi-stage model makes it possible to model the multi-stage process while remaining within process tolerances.

4 Conclusions

This paper presents a study on progressive forming of copper parts with single and complex process coupled with experimental and numerical approach for bending operations for a copper Cu-ETP R290. A single stage bending tool was designed to be representative of more complex geometries. It was used on an industrial press, with load and displacement local sensors, to obtain a large experimental database. Springback magnitude and the local strain states were also measured.

The bending force is mainly influenced by the sample width, it increases when the width increases. The maximum value of the load is found to be proportional to the value of the width. The springback is greater as the bent width increases. The measurement of the strain field by DIC showed that the sample is mainly deformed according to a plane strain condition.

Numerical models of the bending with Abaqus/Standard were developed for each configuration. Sensitivity analyses of the friction coefficient and the clearance between the punch and the sheet allowed a calibration of the input parameters.

The models for the rectangular geometries capture some of the trends from the experiment such as the proportionality of the maximum force with the bent width. The force evolution is rather well predicted for geometries of width 15 mm. The simulation underestimates the force evolution for the geometries of width 5 mm. However, the prediction of the maximum force value remains acceptable.

Overall, the models are able to predict springback within the process tolerance. The increase of springback with the increase of the sample width is also well captured by the simulation.

After having validated the single stage bending model, this work focused on the 3D modelling of an industrial multi-stage process used to produce an electrical contact. The different stages of the process have been studied in terms of strain and geometry with a qualitative and quantitative experimental/numerical validation. The bending sequence involves a calibration stage with a cam slider and rotating punch whose sensitivity could be studied numerically and thus identify a cam position setting that allows to respect the geometric tolerances of the part specifications. Comparison of one stage of the bending sequence with the single stage bending model showed that the single model approach gives similar results in terms of load and plastic deformation. This may show the interest of the single stage bending tool to represent the bending operations occurring in a more complex multi-stage process and thus be useful when using new materials or different batches of the same materials.

Acknowledgements

The authors would like to thank Chantal LE GRAËT, Loïc POUPON and Stephen COROLLER at AXON' MECHATRONICS, Hervé BELLEGOU and Anthony JEGAT at IRDL for their technical support. The authors also aknowledge AXON' MECHATRONICS for technical support and provinding the case studied.

Funding

This work is part of a French collaborative project EXPRESSo (n2017-PSPC-13 of 11/12/2017) with the financial support of Bpifrance.

Conflicts of interest

The authors have nothing to disclose.

Data availability statement

This article has no associated data generated and/or analyzed.

Author contribution statement

Conceptualization, A. Lagroum, P.Y. Manach and S. Thuillier; Methodology, A. Lagroum, P.Y. Manach and S. Thuillier; Validation, A. Lagroum, P.Y. Manach and S. Thuillier; Investigation, A. Lagroum; Writing – Original Draft Preparation, A. Lagroum and S. Thuillier; Writing – Review & Editing, A. Lagroum, P.Y. Manach and S. Thuillier; Project Administration, S. Thuillier; Funding Acquisition, S. Thuillier.

References

[1] F. Gréban, Découpabilité du cuivre et des alliages cuivreux, PhD thesis, Université de Franche-Comté, 2006

[2] K. Bergström, S. Kivivuori, S. Osenius, A. Korhonen, Computer aided design of a progressive die, in: J.L. Chenot, E. Oñate (Eds.), Modelling of Metal Forming Processes, Springer Netherlands, Dordrecht, 1988, pp. 155–162

[3] J.C. Choi, B.M. Kim, C. Kim, An automated progressive process planning and die design and working system for blanking or piercing and bending of a sheet metal product, Int. J. Adv. Manuf. Technol. **15**, 485–497 (1999)

[4] B.C. Hwang, S.M. Han, W.B. Bae, C. Kim, Development of an automated progressive design system with multiple processes (piercing, bending, and deep drawing) for manufacturing products, Int. J. Adv. Manuf. Technol. **43**, 644–653 (2009)
[5] S. Kumar, R. Singh, An automated design system for progressive die, Expert Syst. Appl. **38**, 4482–4489 (2011)
[6] M. Ghatrehnaby, B. Arezoo, A fully automated nesting and piloting system for progressive dies, J. Mater. Process. Technol. **209**, 525–535 (2009)
[7] J. Li, A. Nee, B. Cheok, Integrated feature-based modelling and process planning of bending operations in progressive die design, Int. J. Adv. Manuf. Technol. **20**, 883–895 (2002)
[8] M.A. Farsi, B. Arezoo, V. Alizadeh, S. Mirzaee, The study of spring-back in wipe-bending processes for perforated components, Proc. Inst. Mech. Eng. Part B **225**, 2007–2014 (2011)
[9] S. Tumkor, K. Pochiraju, Progressive die strip layout optimization for minimum unbalanced moments, J. Manuf. Sci. Eng. **132**, 024502 (2010)
[10] S.-B. Sim, S.-T. Lee, C.-H. Jang, A study on the development of center carrier type progressive die for U-bending part process, J. Mater. Process. Technol. **153–154**, 1005–1010 (2004)
[11] D. Farioli, E. Kaya, A. Fumagalli, P. Cattaneo, M. Strano, A data-based tool failure prevention approach in progressive die stamping, J. Manuf. Mater. Process. **7**. 92 (2023)
[12] F. Steinlehner, M. Ott, D. Budnick, A. Weinschenk, S. Laumann, M. Worswick, W. Volk, Development of inline closed-loop vibration control in progressive die stamping using finite element simulation, IOP Conf. Ser. Mater. Sci. Eng. **967**, 012035 (2020)
[13] Y. Gen, W. Yunong, Progressive stamping process and die design of high strength steel automobile structural parts, J. Phys. Conf. Ser. **1605**, 012063 (2020)
[14] G. Ouaidat, A. Lagroum, A. Kacem, S. Thuillier, Uncertainties on the mechanical behaviour of bronze sheets: influence on the failure in bending, Int. J. Mater. Forming **17**, 29 (2024)
[15] C.-L. Huang, M. Xu, S. Cui, Z. Li, H. Fang, P. Wang, Copper-induced ripple effects by the expanding electric vehicle fleet: a crisis or an opportunity, Resources Conserv. Recycl. **161**, 104861 (2020)
[16] A. Mkaddem, D. Saidane, Experimental approach and RSM procedure on the examination of springback in wiping-die bending processes, J. Mater. Process. Technol. **189**, 325–333 (2007)
[17] N. Le Maoût, Analyse des procédés de sertissage de tôles métalliques, PhD thesis, Université de Bretagne-Sud, 2009
[18] A.H. Alghtani, Analysis and optimization of springback in sheet metal forming, PhD thesis, University of Leeds, publisher: University of Leeds, 2015
[19] H. Livatyali, T. Altan, Prediction and elimination of springback in straight flanging using computer aided design methods. Part 1. Experimental investigations, J. Mater. Process. Technol. **117**, 262–268 (2001)
[20] K. Chan, S. Wang, The effect of a coating on the springback of integrated circuit leadframes, J. Mater. Process. Technol. **116**, 231–234 (2001)
[21] M. Fu, K. Chan, W. Lee, L. Chan, Springback in the roller forming of integrated circuit leadframes, J. Mater. Process. Technol. **66**, 107–111 (1997)
[22] D. Briesenick, M. Liewald, Efficient net shape forming of high-strength sheet metal parts by Transversal Compression Drawing, Int. J. Adv. Manuf. Technol. **130**, 3053–3063 (2024)
[23] C. Lange, Étude physique et modélisation numérique du procédé de sertissage de pièces de carrosserie, PhD thesis, École Nationale Supérieure des Mines de Paris, 2006
[24] F. Gassara, R. Hambli, T. Bouraoui, F.E. Halouani, D. Soulat, Optimization of springback in L-bending process using a coupled Abaqus/Python algorithm, Int. J. Adv. Manuf. Technol. **44**, 61–67 (2009)
[25] H. Livatyali, H. Wu, T. Altan, Prediction and elimination of springback in straight flanging using computer-aided design methods. Part 2. FEM predictions and tool design, J. Mater. Process. Technol. **120**, 348–354 (2002)
[26] E. Gildemyn, Caractérisation des procédés de fabrication de pièces de securité automobile. Optimisation multiobjectifs de la mise en forme, Theses, Arts et Métiers ParisTech (Angers), 2008
[27] R. Bahloul, Optimisation of the bending process of high strength low alloy sheet mtetal, PhD thesis, Arts et Métiers ParisTech (Angers), 2005
[28] S. Ben-Elechi, R. Bahloul, A. Potiron, Optimisation des paramètres du procédé de pliage en tombé de bord par plan d'expériences numérique et méthode des surfaces de réponse, Méc. Ind. **7**, 475–485 (2006)
[29] R. Kazan, M. Fırat, A.E. Tiryaki, Prediction of springback in wipe-bending process of sheet metal using neural network, Mater. Des. **30**, 418–423 (2009)
[30] F. Adzima, T. Balan, P.Y. Manach, Springback prediction for a mechanical micro connector using CPFEM based numerical simulations, Int. J. Mater. Forming **13**, 649–659 (2020)
[31] F.-K. Chen, S.-F. Ko, Deformation analysis of springback in L-bending of sheet metal, J. Achiev. Mater. Manuf. Eng. **18** (2006)
[32] H.H. Bok, K.S. Oh, Y.S. Kang, Simulation of springback in cyclic wipe-bending, IOP Conf. Ser. Mater. Sci. Eng. **967**, 012073 (2020)
[33] R. Bahloul, A. Mkaddem, P. Dal Santo, A. Potiron, D. Saïdane, Optimisation du procédé de pliage pour la mise en forme de pièces de sécurité automobile, Eur. J. Computat. Mech. **17**, 323–348 (2008)
[34] M.C. Oliveira, D.M. Neto, A. Pereira, J.L. Alves, L. Menezes, Evaluating the influence of the deformation of the forming tools in the thickness distribution along the wall of a cylindrical cup, IOP Conf. Ser. Mater. Sci. Eng. **1238**, 012079 (2022)
[35] A. Lagroum, Conception virtuelle de la mise en forme progressive d'alliages de cuivre pour des applications électroniques, PhD thesis, Université Bretagne Sud, 2022
[36] J.L. Jordan, C.R. Siviour, G. Sunny, C. Bramlette, J.E. Spowart, Strain rate-dependant mechanical properties of OFHC copper, J. Mater. Sci. **48**, 7134–7141 (2013)
[37] C. Durand, H. Song, R. Bigot, Parametric identification on a dynamic behavior model for a forging machine, in: Materials Research Proceedings 28, 2023, pp. 649–656
[38] T. Xu, Q. Xia, X. Long, G. Buffa, Vibration Control of a High-Speed Precision Servo Numerically Controlled Punching Press: Multidomain Simulation and Experiments, Shock and Vibration 2017, 2017 pp. 1–17

[39] F. Jia, F. Xu, Dynamic analysis of closed high-speed precision press: modeling, simulation and experiments, Proc. Inst. Mech. Eng. Part C **228**, 2383–2401 (2014)
[40] International Digital Image Correlation Society, E. Jones, M. Iadicola, R. Bigger, B. Blaysat, C. Boo, M. Grewer, J. Hu, A. Jones, M. Klein, K. Raghavan, P. Reu, T. Schmidt, T. Siebert, M. Simenson, D. Turner, A. Vieira, T. Weikert, A Good Practices Guide for Digital Image Correlation, Tech. rep., 1st edn.,International Digital Image Correlation Society, 2018

Cite this article as: A. Lagroum, P.-Y. Manach, S. Thuillier, From single to multi-stage forming process of copper thin sheet, Mechanics & Industry **26**, 4 (2025), https://doi.org/10.1051/meca/2024039

Appendix A:

The configuration of the image stereo-correlation system (Aramis 3D), as well as the analysis parameters used to calculate the fields, are presented in Table A.1. Noise was measured on the basis of a set of 20 images recorded with no load. Then, an average measurement of the ε_1 and ε_2 strains on a surface (2.5 mm × 15 mm) is made for each image. A global average over the 20 images is then calculated, which is the value of the error on the strain measurement.

Table A.1. System and parameters for image stereo-correlation analysis (Aramis 3D) for single stage bending tests, table proposed by [40].

Camera	ARAMIS 4M
Image resolution	2352 × 1728 pixels^2
Lens (focal length)	50 mm
Field-of-View/Measuring volume	55 × 40 × 25 mm^3
Image Scale	35.1 pixels/mm
Stereo-Angle	26.6°
Stand-off Distance	260 mm
Subset Size	18 pixels/0.512 mm
Step Size	6 pixels/0.171 mm
Strain Noise-Floor on ε_1	420 µm/m
Strain Noise-Floor on ε_2	470 µm/m